Available online at www.sciencedirect.com
ScienceDirect
Ocean Modelling 17 (2007) 300–326
Ocean Modelling
www.elsevier.com/locate/ocemod

Bred-ensemble ocean forecast of loop current and rings

X.-Q. Yin [1], L.-Y. Oey *

Princeton University, NJ, USA

Received 10 November 2006; received in revised form 9 February 2007; accepted 26 February 2007
Available online 12 March 2007

Abstract

Ocean forecasting with a General Circulation Model (GCM) commonly begins from an initial analysis obtained by data assimilation. Instead of a single initial state, bred-ensemble forecast [BEnF; which is used for weather forecasting at the National Centers for Environmental Prediction] begins from an ensemble of initial states obtained by using the GCM to breed fast-growing modes into the analysis. Here we apply the technique to forecast the locations and strengths of the Loop Current and rings from July through September 2005. Model results are compared against satellite observations, surface drifter trajectories, and moored currents. It is found that BEnF gives closer agreements with observations than the conventional single forecast. The bred-vectors (perturbed minus unperturbed state-vectors) have growth rates ≈0.04–0.08 day^{-1} and spatial (cyclone–anticyclone) scales ≈200–300 km suggestive of baroclinic instability mode in the Loop Current and rings. As in atmospheric applications, initializations with these growing vectors contribute to the more accurate ensemble mean forecast.

Keywords: Bred-ensemble forecast; Ocean circulation; Loop current; Rings

Regional Index Terms: Gulf of Mexico; Caribbean Sea

1. Introduction

The Loop Current is the dominant feature of the circulation in the eastern Gulf of Mexico and the formation region of the Florida Current-Gulf Stream system (Figs. 1 and 2). It originates at the Yucatan Channel through which approximately 23–27 Sv (1 Sv = 10^6 m^3 s^{-1}) transport passes with a large minimum–maximum range of 14–36 Sv (Johns et al., 2002; Sheinbaum et al., 2002). Peak speeds of 1.5–1.8 m s^{-1} have been observed near the surface in the Loop Current (e.g., Nowlin, 1972; Forristal et al., 1992; see Oey et al., 2005a for other references). The Loop Current feeds the Florida Current which transports significant amounts of heat poleward. The Loop episodically sheds warm-core rings (e.g., Cochrane, 1972; Vukovich, 1995) at intervals of approximately 3–18 months (Sturges and Leben, 2000; Leben, 2005). These rings have diameters

* Corresponding author. Tel.: +1 609 258 5971.
E-mail address: lyo@princeton.edu (L.-Y. Oey).
[1] Also at First Institute of Oceanography, Qingtao, China.

1463-5003/$ - see front matter © 2007 Elsevier Ltd. All rights reserved.
doi:10.1016/j.ocemod.2007.02.005

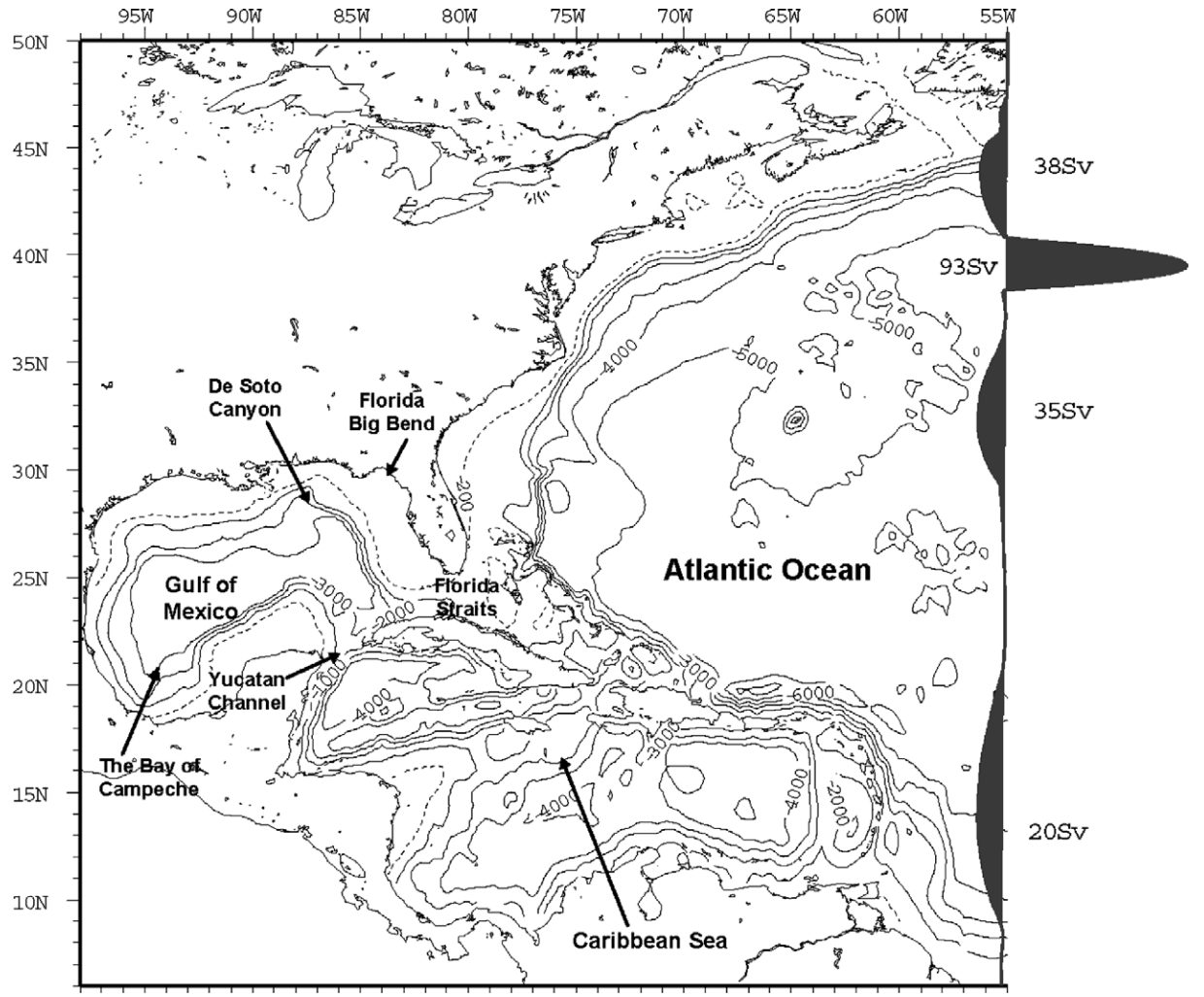

Fig. 1. A locator map of the study region: the Gulf of Mexico and surrounding ocean regions. The domain shown is also the model domain. Time-independent inflow and outflow that account for the large-scale transports (Svedrup + thermohaline) are specified across the open boundary at 55 °W as a function of latitude (as indicated with silhouette profiles). Contours show isobaths in meters.

≈200–300 km, vertical extent ≈1000 m, and swirl speeds ≈1.8–2 m s^{-1}; they generally translate westward at 2–5 km day^{-1} and have lifetimes of months to approximately a year (Nowlin, 1972; Elliott, 1982; Vukovich and Crissman, 1986; Cooper et al., 1990; Forristal et al., 1992). The Loop Current and its rings are powerful oceanic features that affect, either directly or indirectly through their smaller-scale subsidiaries, just about every aspect of oceanography of the Gulf (Oey et al., 2005a).

In addition to producing strong ocean currents, the Loop and rings possess, by virtue of their deep thermoclines, large values of the Ocean Heat Content (OHC; Leipper and Volgenau, 1972):

$$\mathrm{OHC} = \rho_0 C_p \int_{Z_{26}}^{\eta} (T - 26)\mathrm{d}z, \quad T \geqslant 26\,^{\circ}\mathrm{C},$$

where Z_{26} (>0) is depth of the 26 °C isotherm, η = sea-surface height (SSH), ρ_0 density of sea water and C_p the specific heat of water. Sea surface temperatures (SST's) in excess of 26 °C are necessary for tropical cyclogenesis (Palmen, 1948; DeMaria and Kaplan, 1994). Regions where OHC > 60–90 kJ/cm^2 have been empirically found to be conducive to storm intensification, and OHC has been used as one of several parameters in hurricane prediction schemes (DeMaria et al., 2005). Typical values of OHC in summer through autumn easily

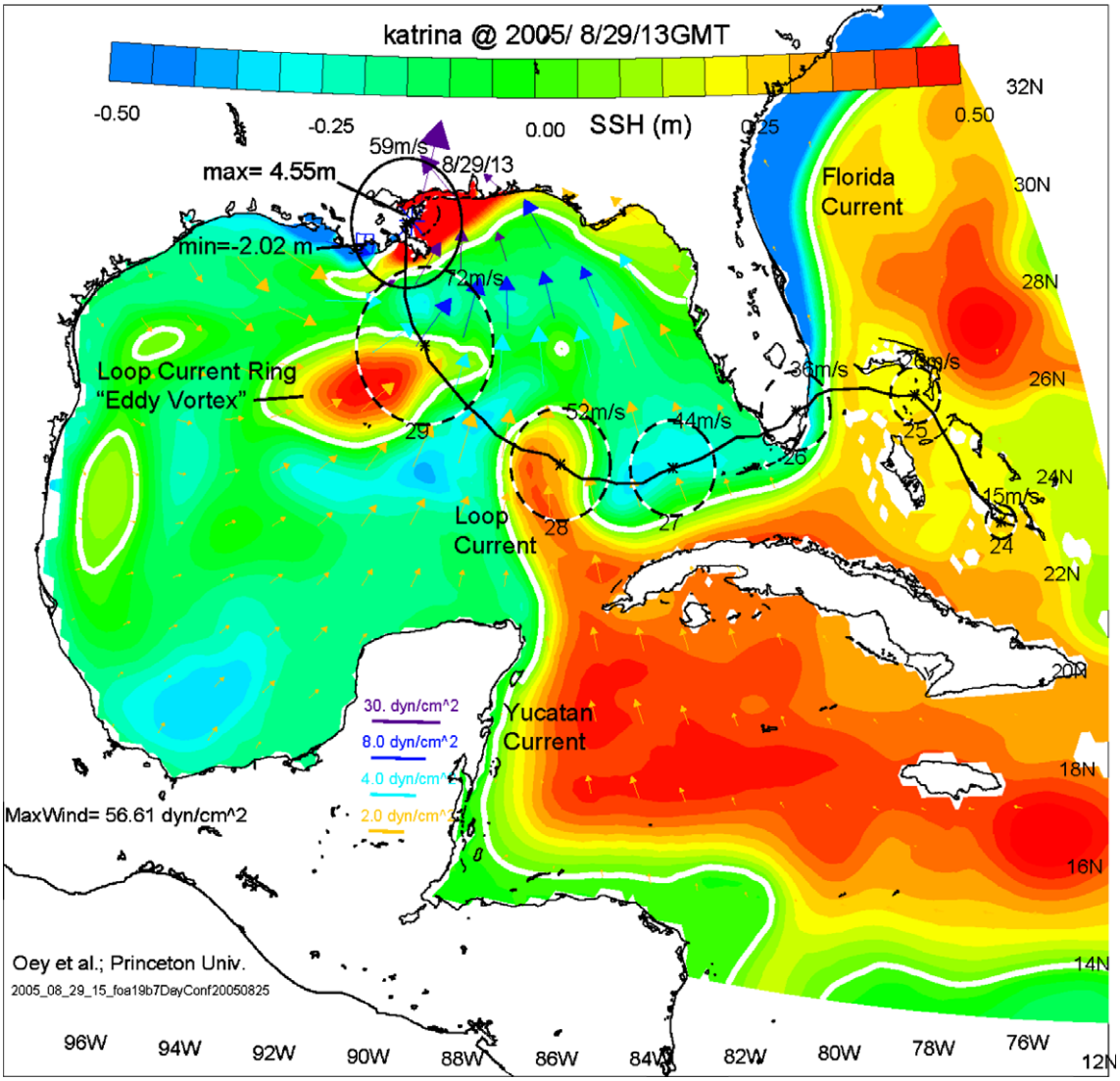

Fig. 2. An illustrative figure of the Loop Current and its associated ring during the study period. Shown here in color is the forecast (ConF) sea-surface height (SSH; white contour is SSH = 0) on Aug/29/13GMT just after Hurricane Katrina made landfall (solid circle) at New Orleans. Note the high SHH (red; max ≈4.6 m) near New Orleans. The storm's path is shown as solid black line and its intensities are shown proportional to the size of circles (dashed) plotted at daily intervals beginning at Aug/24. Colored vectors indicate wind stresses with the indicated scales.

exceed 60 kJ/cm^2 within the Loop and rings (e.g., Oey et al., 2006; Oey et al., in press). Scharroo et al. (2005) suggest that the large heat contents of the Loop and a ring (which is named "Eddy Vortex") during hurricane *Katrina* (*Aug/23–30/2005*) may have resulted in the rapid intensification of the storm (Fig. 2).

It is therefore of scientific and practical values to accurately forecast (and hindcast) the locations, paths and strengths of the Loop Current and rings. In this work, by forecast we mean forward model integration without data assimilation. Oey et al. (2005b) compared fourteen *4-week* forecasts of Loop Current and rings' frontal positions against observations for the period *Aug/1999* through *Sep/2000*. Each forecast was initialized from a data-assimilative analysis field which in this work will be referred to as the control analysis (ConA; see Appendix 1 for explanations of acronyms and variables). Their model (which was based on the Princeton Ocean Model or POM, see below) correctly predicted the separation of a powerful ring from the Loop Current three weeks in advance. The mean frontal position errors ≈25 km while the root-mean-square (RMS) errors

≈50 km over the four-week forecast horizon. The authors suggested that the largest contributor to the forecast errors was error in the initial ConA field.

Oey et al. (2005b) utilized the methodology commonly used in ocean forecasting: one first initializes the model from a ConA field, and then integrates the model forward. This type of forecast will be referred to as the control forecast (ConF). In this work, instead of a single forecast initialized from one analysis field, we conduct an ensemble of forecasts with initial fields obtained using the breeding method (Toth and Kalnay, 1997). An eight-week forecast horizon is chosen, from end of *July* through the middle of *September 2005*. This period coincides with the passage of hurricane *Katrina – Aug/23–30/2005*. As depicted in Fig. 2, there was a large sea-level (maximum $\eta = 4.5$ m) setup along the Mississippi-Alabama coast when *Katrina* made land-fall at the northern Gulf coast. The storm breached the levees that protected New Orleans from Lake Pontchartrain, and most of the city was subsequently flooded, causing considerable human suffering and property losses. Although accurate wind field for *Katrina* is included in our forecast, short-time ocean currents and waves produced by the hurricane will not be our main focus here. This work concentrates instead on estimating the positions and strengths of the Loop Current and ring(s). The goal is to compare the skills of the conventional forecast (i.e., ConF) versus bred-ensemble forecast (i.e., BEnF) through direct comparison with observations.

We describe the model, forcing and assimilation method in Section 2. Breeding and ensemble forecasting are described in Section 3, where we also discuss bred vectors (perturbed minus unperturbed state-vectors). In Section 4 we compare our results against (i) sea-surface height anomaly (SSHA) from satellite, (ii) trajectories of a NOAA/AOML hurricane drifter (http://www.aoml.noaa.gov/phod/dataphod/work/trinanes/INTERFACE/index.html), and (iii)Acoustic Doppler Current Profiler (ADCP) measurements. Section 5 concludes the paper.

2. The model, wind forcing, control analysis and forecast

2.1. The model

Our circulation model for the Caribbean Sea and the Gulf of Mexico is based on the Princeton Ocean Model (Mellor, 2004), and has been tested for process studies as well as in realistic simulations (Oey and Lee, 2002; Ezer et al., 2003; Wang et al., 2003; Fan et al., 2004; Oey and Zhang, 2004; Oey, 2004; Oey et al., 2003, 2004, 2005a,b, 2006, in press). A brief description is given below.

The model domain includes the northwestern Atlantic Ocean west of 55° W as shown in Fig. 1. At 55° W, estimates of inflow and outflow transports are specified in combination with radiation conditions. The baroclinic velocities are specified using the radiation conditions. Climatological temperature and salinity are specified during inflow and advected out using one-sided differencing at outflow. Details of open boundary conditions are in Oey and Chen (1992). The model is forced by wind to be detailed below, as well as by monthly discharges from 34 rivers along the northern Gulf coast according to the method given in Oey (1995, 1996). The model horizontal grid-size is variable; it is approximately 10 km in the Loop Current and northwestern Caribbean Sea, and about 5 km in the northeastern Gulf of Mexico. There are 25 terrain-following (the so-called *sigma*-coordinate) layers with 10 of them in the top 250 m for local water depth ≈2500 m. The Mellor and Yamada's (1982) turbulence closure scheme modified by Craig and Banner (1994) to effect wave-enhanced turbulence near the surface is used. To account for mixing in stable stratification (e.g., internal waves; MacKinnon and Gregg, 2003; Mellor's, 2001) modification of a Richardson-number-dependent dissipation is used. In this work, surface heat and evaporative fluxes are set to zero so that the SST variations are due to model's internal dynamics; in the case of forcing by a hurricane, Price (1981) found that surface cooling by these fluxes is small compared to cooling by mixing.

2.2. The wind

We combine the analyzed winds from the Hurricane Research Division [HRD; http://www.aoml.noaa.gov/hrd/] with the National Centers for Environmental Prediction's [NCEP] global wind analysis (the Global Forecast System winds; Caplan et al. (1997)). The HRD data is given in a 1000 km × 1000 km (dimensions

are approximate) moving "box" centered about the hurricane's track. Storm centers are first linearly interpolated to hourly locations. Consecutive HRD maps are then overlapped at the hourly locations and linearly interpolated. The hourly maps are then merged with NCEP wind using a weight that retains the HRD data within a circle of radius = 0.8 side of the box (i.e., ≈400 km), and that smoothly (using a tanh function) merges the HRD and NCEP winds beyond that radius. Animations of both the HRD and HRD/NCEP merged winds are posted on our web-site: http://www.aos.princeton.edu/WWWPUBLIC/PROFS/animations.html. Fig. 3 shows the merged winds for *Katrina* (*Aug/24–29/2005*). To calculate wind stresses, we use a bulk formula with a high wind-speed limited drag coefficient that fits data for low-to-moderate winds (Large and Pond, 1981) and data for high wind speeds (Powell et al., 2003), as given in Oey et al. (2006):

$$\begin{aligned} C_d \times 10^3 &= 1.2, \qquad |\boldsymbol{u}_a| \leqslant 11 \text{ m s}^{-1} \\ &= 0.49 + 0.065|\boldsymbol{u}_a|, \quad 11 < |\boldsymbol{u}_a| \leqslant 19 \text{ m s}^{-1} \\ &= 1.364 + 0.0234|\boldsymbol{u}_a| - 0.00023158|\boldsymbol{u}_a|^2, \quad 19 < |\boldsymbol{u}_a| \leqslant 100 \text{ m s}^{-1}, \end{aligned} \tag{1}$$

where $|\boldsymbol{u}_a|$ is the wind speed.[2] The maximum cut-off at 100 ms^{-1} is at present adequate even for an intense hurricane such as Katrina. According to this formula, C_d is constant at low winds, is linearly increasing for moderate winds, reaches a broad maximum for hurricane-force winds, $|\boldsymbol{u}_a| \approx 30$–$50$ m s^{-1}, and then decreases slightly for extreme winds. Donelan et al. (2004) suggest that the C_d-leveling at high wind may be caused by flow separation from steep waves. Moon et al. (2004) found that C_d decreases for younger waves that predominate in hurricane-forced wave fields. Bye and Jenkins (2006) attribute the broad C_d-maximum to the effect of spray, which flattens the sea surface by transferring energy to longer wavelengths.

2.3. Data assimilation and control analysis (ConA)

We assimilate satellite SSHA ($\delta\eta_0$, from AVISO, www.aviso.oceanobs.com; Ducet et al., 2000) and SST (from the United States GODAE, www.usgodae.org) to derive ConA to initialize the model forecast. Satellite data are assimilated into the model following the methodology given in Mellor and Ezer (1991) and Ezer and Mellor (1994). In this method, SSHA is projected into the subsurface temperature field using pre-computed correlation factors derived from a long-time (≈10 years) prognostic integration that has yielded a statistical equilibrium eddy field. Thus the resulting temperature anomaly (δT) is ($\langle\cdot\rangle$ is time-averaging, and T is the potential temperature):

$$\delta T(x,y,z,t) = F_T(x,y,z)\delta\eta_0(x,y,t), \tag{2}$$

where the correlation factor is ($\delta\eta$ = model SSHA)

$$F_T = \langle \delta T \delta\eta \rangle / \langle \delta\eta^2 \rangle, \tag{3a}$$

and the corresponding correlation coefficient is

$$C_T = \langle \delta T \delta\eta \rangle / [\langle \delta T^2 \rangle \langle \delta\eta^2 \rangle]^{1/2}. \tag{3b}$$

Ezer and Mellor (1994) assimilate along-track $\delta\eta_0$ data assuming a linear-saturation error growth model for the first-guess error. Our experience has been that if AVISO $\delta\eta_0$ maps are assimilated the following simplified formula (due originally to Ezer et al., 2003, private communication; see Wang et al., 2003) suffices:

$$T^a = T + [2R_A C_T^2/(1 + 2R_A C_T^2 - C_T^2)](T_O - T) \tag{4}$$

where T is the model (first-guess) temperature, T^a denotes the analysis temperature, R_A is the ratio of the assimilated time step Δt_A to the de-correlation time scale Δt_E of the model eddy field, and T_O is the 'observed' temperature inferred from (2),

$$T_O = \langle T \rangle + F_T \delta\eta_0. \tag{5}$$

[2] In Oey et al. (2006), the coefficient for $|\boldsymbol{u}_a|^2$ was erroneously rounded off to 0.0002.

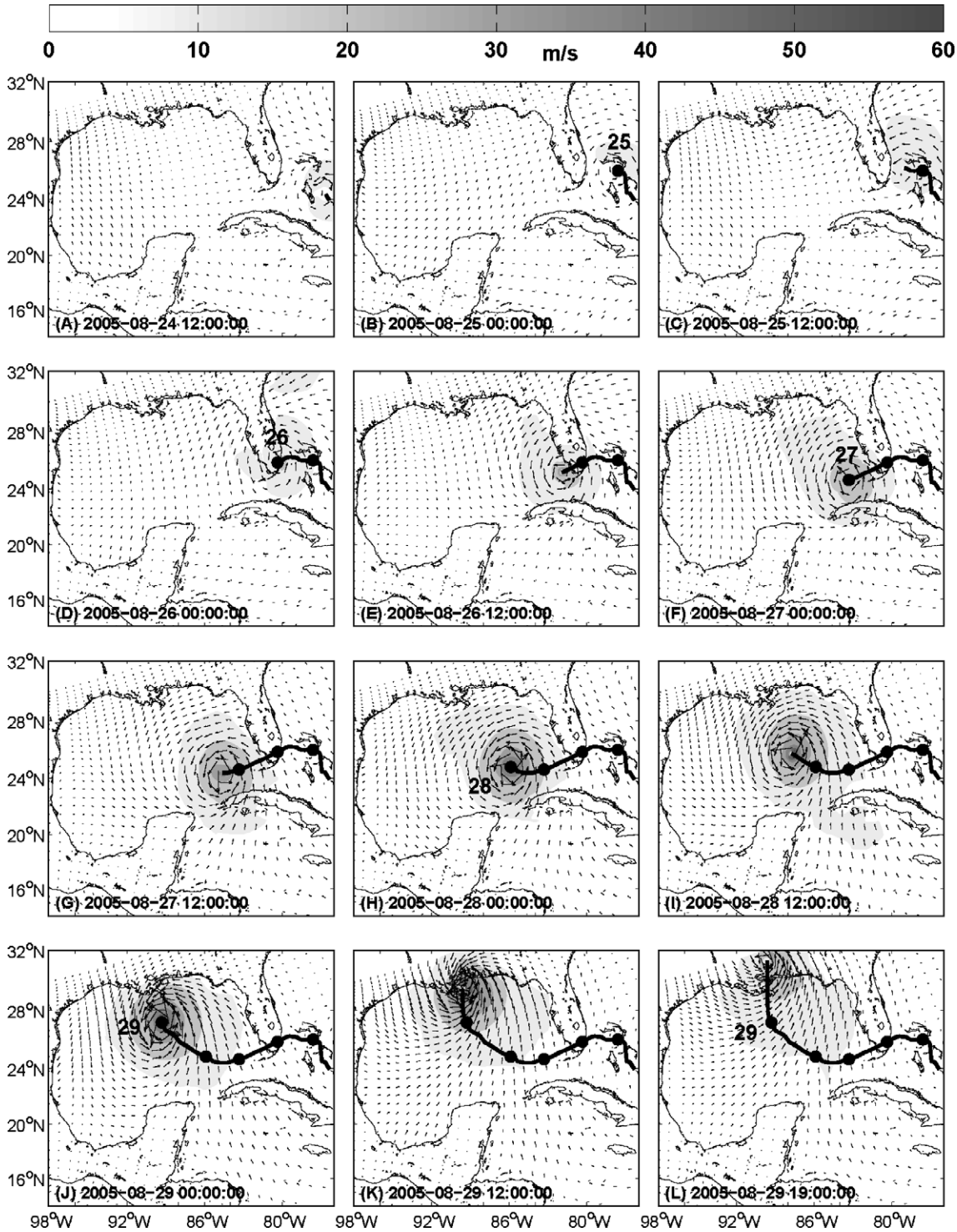

Fig. 3. Twelve-hourly plots of HRD/NCEP winds showing the path of hurricane *Katrina* from (A) Aug/24/12:00 through (K) 29/12:00/2005. The last panel (L) is for Aug/29/19:00. Dots indicate daily locations of the storm's eye.

Instead of using the model mean for $\langle T \rangle$ in (5), our past experience has been that setting $\langle T \rangle = T_C$, the observed temperature climatology, helps to control long-term ($\sim$10 years) drift in the model. For the present

application, the differences are small. Formula (4) assumes that the AVISO map errors are small compared to the model errors, and that $\Delta t_A << \Delta t_E$. We follow Ezer and Mellor (1994) and set $\Delta t_A = 1$ day. The Δt_E is estimated from the above-mentioned 10-year prognostic model run and is ≈30 days in regions of the Gulf of Mexico dominated by the Loop Current and rings. This may be compared with the value of 20 days used by Ezer and Mellor's (1994) for the Gulf Stream which therefore appears to have shorter meander and eddy evolution time scales. The Δt_E is also proportional to the time scale of the model error growth, and the 30-day value is consistent with Oey et al.'s (2005b) findings of predictability time scales of about one month for the Loop Current and its associated rings. As pointed out by Ezer and Mellor (1994), the assimilation (4) is such that $T^a \approx T_O$ in regions where the correlation is high ($C_T^2 \approx 1$), but $T^a \approx T$ where the correlation is low. A similar assimilation of SST is also carried out after (4) with C_T and F_T replaced by the corresponding functions that use δ(SST) in place of $\delta\eta$ in (3). The SSHA and SST assimilations complement each other: SSHA assimilation is most effective over deep waters (for isobath > 500 m) while SST assimilation influences waters on shallow shelves. For more details see Wang et al. (2003), Fan et al. (2004) and Oey et al. (2005b).

Using the assimilation procedure above, we produce daily ConA fields from *May/26* through *Nov/17/2005*.

2.4. Control (unperturbed) forecasts (ConF)

We define ConF to be a model run that is free from any data assimilation and that is initialized from a ConA field. Two *8-week* forecasts, *Jul/21–Sep/15* and *Jul/28–Sep/22/2005* are conducted to cover different periods for comparison with observations (below). The two runs give similar results during their overlapped period. These initial dates are about one month prior to the date when *Katrina* made landfall in the northeastern Gulf of Mexico on *Aug/29/2005*. The same forecast periods are used for the ensemble forecast experiments, described next.

3. The breeding method and bred-ensemble forecast (BEnF)

Toth and Kalnay (1993, 1997; see also Chapter 6 of Kalnay, 2003) develop the breeding method and describe its application to atmospheric ensemble forecasting. We outline their ideas modified for the present oceanic application; readers should consult their works for details. Leith (1974) showed that in a perfect model environment averaging the ensemble forecasts yields a mean forecast superior (in the sense of smaller RMS error) to the control forecast, provided that the ensemble perturbations are representative of the span of possible errors in the initial analysis (ConA). The ConA contains, in addition to the random observational errors, growing errors associated with the instabilities of the evolving flow. This is because for the first guess the analysis repeatedly uses the model forecast ("T" in Eq. (4)), which after some time diverges from the analysis (an approximation of the true state) (Lorenz, 1963; Lorenz, 1965; Lorenz, 1993). In other words, forecast errors are dominated by the fastest growing ones due to flow instability (Lorenz, 1965). These dominant errors are called "singular modes" in modern terminology (Kalnay, 2003, Chapter 6). At each analysis cycle, the errors are reduced in size because of new observations, but are not eliminated. These dynamically developed errors are therefore present at the next analysis cycle ready to amplify again, i.e., they represent the uncertainty in ConA. The breeding method mimics the analysis cycle and generates perturbations along the initial error pattern as in the following descriptions.

Let the daily analysis at time "n" (the nth day) of the state vector "T" (e.g., T = the grid-point temperatures) be $T^a(n)$, $n = 0,1,2,\ldots,KN$, where $n = 0$ is some (reference) past time, K is an integer that denotes the total number of breeding cycles (see below), and N is the number of days per cycle; thus the time $t = KN$ days will be the forecast start time. The goal is to generate an ensemble of perturbed state vectors $T_m(n = KN)$, $m = 1,2,\ldots,M$, that contain the aforementioned fast growing modes, and that are then used as initial conditions for ensemble forecasts. Here, M = total number of ensemble members used, superscripts "a" and "f" (see below) denote analysis and forecast respectively, and the subscript "m" indicates a perturbed variable as well as the mth member of the ensemble; also, time dependence only is indicated inside the parentheses following a variable, the spatial dependence is omitted. The method consists of the following steps (Fig. 4):

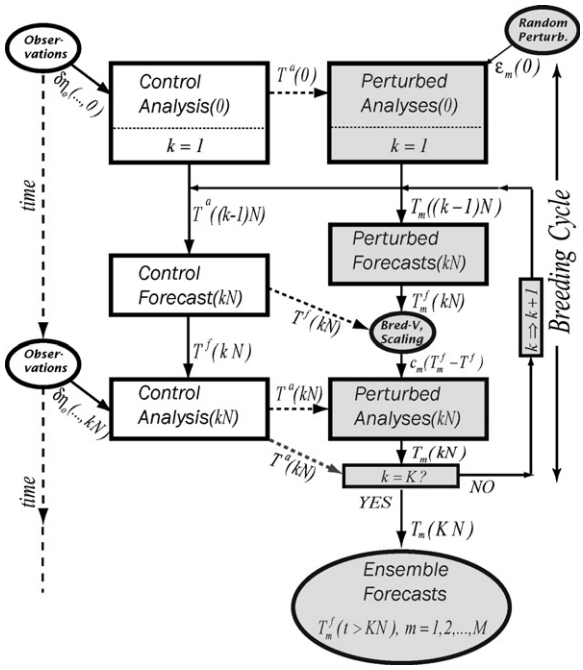

Fig. 4. A flow chart that describes the breeding cycle and ensemble forecasting. The flow diagram shown on the left-hand side is the conventional analysis-and-forecast cycle. The breeding cycle of ensemble forecasting is indicated by shaded flow boxes and ellipses on the right.

(a) At time $t = 0$ $(=n)$, add a small arbitrary perturbation $\varepsilon_m(0)$ to $T^a(0)$: $T_m(0) = T^a(0) + \varepsilon_m(0)$, $m = 1, 2, \ldots, M$, to form M perturbed analyses. Then integrate the model forward without data assimilation (i.e., forecast) for N days using the perturbed and unperturbed analyses, $T_m(0)$ and $T^a(0)$ respectively ($k = 1$ in Fig. 4). Denote the resulting M perturbed forecasts by $T^f_m(N)$, $m = 1, 2, \ldots, M$, and the single unperturbed forecast as $T^f(N)$. Note that $T^f(N)$ is just ConF at time "N".

(b) Subtract the unperturbed forecast $T^f(N)$ from each of the M perturbed forecasts $T^f_m(N)$, to obtain M perturbation vectors at time N: $\varepsilon_m(N) = c_m(N)(T^f_m(N) - T^f(N))$, where for each m the $c_m(N)$ is a factor that scales the RMS of $\varepsilon_m(N)$ over the phase space to equal the initial RMS of $\varepsilon_m(0)$ (this initial RMS will be set to be the same constant for all M members). Here, by phase space we mean the grid points where the initial perturbations in step (a) are introduced. Form the new perturbed analysis vectors at time N:$T_m(N) = T^a(N) + \varepsilon_m(N)$, $m = 1, 2, \ldots, M$.

(c) Integrate the model forward (without data assimilation) to the next N days from $n = N$ through $n = 2N$ using the perturbed and control analyses at time N obtained from step (b), $T_m(N)$ and $T^a(N)$ respectively (in Fig. 4, increase k by 1, i.e., k becomes 2, and loop back). The resulting M perturbed forecasts are $T^f_m(2N)$, $m = 1, 2, \ldots M$, and the unperturbed forecast is $T^f(2N)$.

Steps (b) and (c) are repeated to obtain at $t = KN$ days the unperturbed vector $T^f(KN)$, all M members of the perturbed vectors $T^f_m(KN)$, hence the scaled perturbations $\varepsilon_m(KN)$, and finally the control and perturbed analysis vectors $T^a(KN)$ and $T_m(KN)$, respectively (last loop in Fig. 4, with $k = K$). Toth and Kalnay (1997) argue that after the breeding cycle the perturbed analysis vectors $T_m(KN)$ are dominated by growing modes each of which is a combination of the fastest-growing singular modes of the nonlinear system; in other words, the ensemble perturbations $\varepsilon_m(KN)$ are contained in the subspace of the probability distribution of the ocean state about our best estimate $T^a(KN)$. The authors show that the breeding method gives ensemble mean that is superior to randomly generated ensemble forecasts. Their results agree with Ehrendorfer and Tribbia (1997) who found that the fastest growing combinations of possible analysis errors give the best results as initial ensemble perturbations for at least the short-range forecasts.

The growing modes can be seen in plots of the bred vectors $\boldsymbol{BV} = T_m^f(n) - T^f(n)$, i.e., the difference between perturbed and unperturbed forecasts (Yang et al., 2006). For example, Fig. 5a shows spatial contours for $\boldsymbol{BV}$ member# 12, and Fig. 5b (upper panel) shows temporal evolutions of spatially averaged amplitudes ("A_m") for different members. In these calculations, $N = 7$ (7-day breeding cycle) and $K = 10$ (total of 10 cycles). The growth rate (GR_k) for the kth-cycle in the lower panel of Fig. 5b is defined as $GR_k = ln[A_m(kN)/A_m((k-1)N)]/N$, $k = 1, 2, \ldots,, K$. The $\boldsymbol{BV}$ in Fig. 5a is near the peak-growth of the breeding cycle (i.e., $k = 7$, Fig. 5b); other members show similar patterns of cyclones and anticyclones (cf. Yang et al., 2006). The initial patterns in step (a) above consist of random fields (specified; see below) which decay during the first cycle (Fig. 5b). Following each breeding cycle, the cyclonic-anticyclonic patterns of Fig. 5a grow, and they mature after the 6–7th cycle shown. The organized structures have large amplitudes in the vicinity of the Loop Current and rings; they have wavelengths of approximately 200–300 km and $GR_k \approx 0.04$–$0.08\ \text{day}^{-1}$. The wavelengths and growth rates strongly indicate that they are baroclinic instability mode of the system.

3.1. Bred-ensemble forecast

Based on an examination of the bred vectors (e.g., Fig. 5), we choose $N = 7$ (7-*day* breeding cycle), $K = 8$ (total of 8 cycles), and $M = 20$ (20 ensemble members). The bred vectors achieve near-maximum growths in about 8 breeding cycles (Fig. 5b) and the time scales are consistent with typical estimates for baroclinically unstable waves in the ocean, about 10 days or less (Wang, 1993). We have also tested $M = 10$, 30 and 50, and found little differences in the ensemble means when $M \approx 20$ or greater. Since our analysis scheme (see above section for ConA) calculates $T^a(n)$ by assimilating $\delta\eta_0$ from satellite, we follow Miyazawa et al.

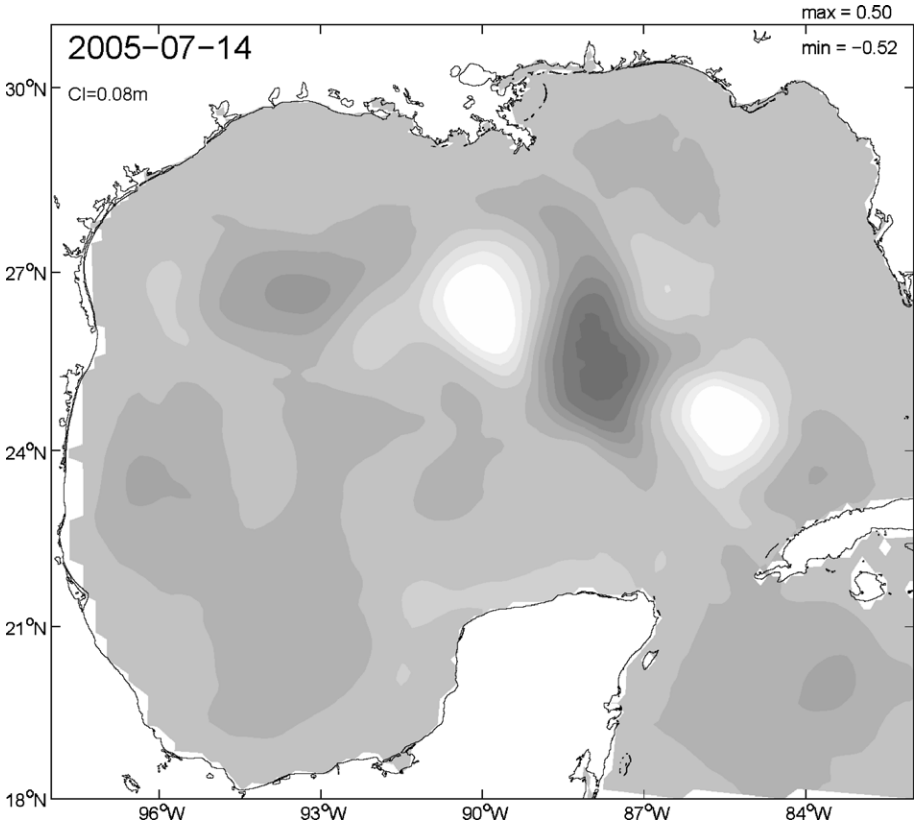

Fig. 5a. Example of a bred vector (member #12) in terms of sea-surface height at Jul/14/2005 near the peak of its growth (see next figure). Darkest shade $\geqslant +0.4$ m and lightest shade $\leqslant -0.4$ m.

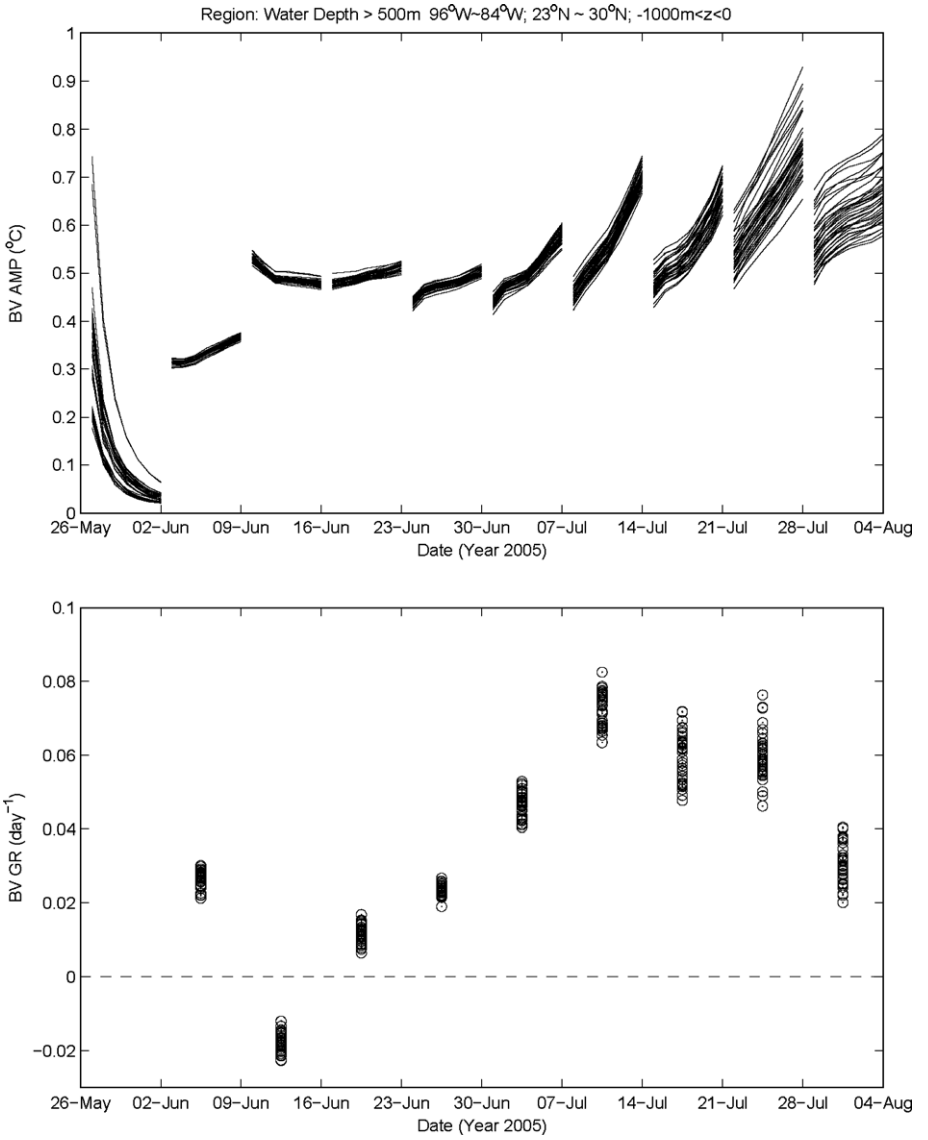

Fig. 5b. Bred vector amplitudes in terms of temperature averaged over the indicated region (upper panel) and the corresponding growth rate (lower panel) for 10 breeding cycles each of 7 days.

(2005; who also use a similar scheme based on Mellor and Ezer, 1991) and replace in steps (a)–(c) above the $T^f_m(n)$ by $F_T\delta\eta^f_m(n)$, and the $T^f(n)$ by $F_T\delta\eta^f(n)$, where F_T is given by (3a) and $\delta\eta^f_m(n)$ and $\delta\eta^f(n)$ are respectively the perturbed and unperturbed forecast SSHA's at the nth *day*. However, $T^f_m(n)$ and $T^f(n)$ are available at each n, and future work may test the option of directly using them. For the RMS of $\varepsilon_m(0)$, it should be large enough to excite linear instability, but not too large that the perturbations lead to solutions that are saturated with finite-amplitude waves, since that would defeat our objective of breeding the growing modes. Kalnay, 2003, *personal communication*) recommended a value $\approx < 10\%$ of the magnitude of the state-vector, and we use RMS $(\varepsilon_m(0)) = 0.07$ m ($|\text{SSHA}| \approx 1$ m). As in Miyazawa et al. (2005), we also specify the initial random perturbation (i.e., $\varepsilon_m(0)$) using Evensen's (1994) pseudo random field with a horizontal correlation scale of 0.7°. Toth and Kalnay's (1993) experience and the ***BV*** plots shown in Fig. 5 suggest however that the particular details of $\varepsilon_m(0)$ is not crucial. Also, when computing the bred vector in step "b" above, Miyazawa et al. (2005) appear to have used "the assimilation run," i.e. the SSHA that corresponds to $T^a(n)$ derived from

ConA, in place of the $\delta\eta^f(n)$ we use. The difference should be small since bred vectors strongly project onto the growing modes of the analysis (Toth and Kalnay, 1997).

As in the ConF experiments, two *8-week* ensemble forecasts, *Jul/21–Sep/15* and *Jul/28–Sep/22/2005* are conducted to cover different periods for comparison with observations (below). The two ensemble forecasts give similar results during their overlapped period. The bred-ensemble forecast is called BEnF, the corresponding ensemble breeding is EnB (i.e. steps "a" through "c" above) and the ensemble mean forecast and breeding are EnMF and EnMB, respectively. For references, Appendix 1 lists these and other acronyms and variables.

4. Comparisons with observations

One way for assessing the "goodness" of a forecast is to conduct twin experiments (examples are given in Anderson et al., 1996). In such an assessment, the results from a control run are treated as "observations" which are then used to assimilate into and compared against a different run (initialized differently, say). The advantage is that we then have at our disposal "observations" of every modeled variable in the entire (model) space-time domain. The drawback is that the "observations" and model are not independent of each other. The method is therefore well-suited for testing assimilation schemes but may not produce reliable measures of forecast skills. Another way is to compare the model (e.g., forecast) against an analysis that is the most complete, thereby treating the latter as "observations." A recent example of this approach is Miyazawa et al. (2005). However, it is clear that this way of assessment lessens but does not entirely eliminate the problem of model and observation inter-dependency. The third way is to use observations to assess the analysis or forecast (Wang et al., 2003; Kamachi et al., 2004; Oey et al., 2004, 2005a, 2006, in press; Oke et al., 2002; Paduan and Shulman, 2004). Clearly, comparisons against observations are the ultimate way one should judge if a forecast is any good. In this section, we compare both analyses and forecasts against observations: (a) satellite SSHA; (b) NOAA drifter trajectories; and (c) ADCP measurements over the northeastern slope of the Gulf of Mexico. Fig. 6 shows the ADCP locations.

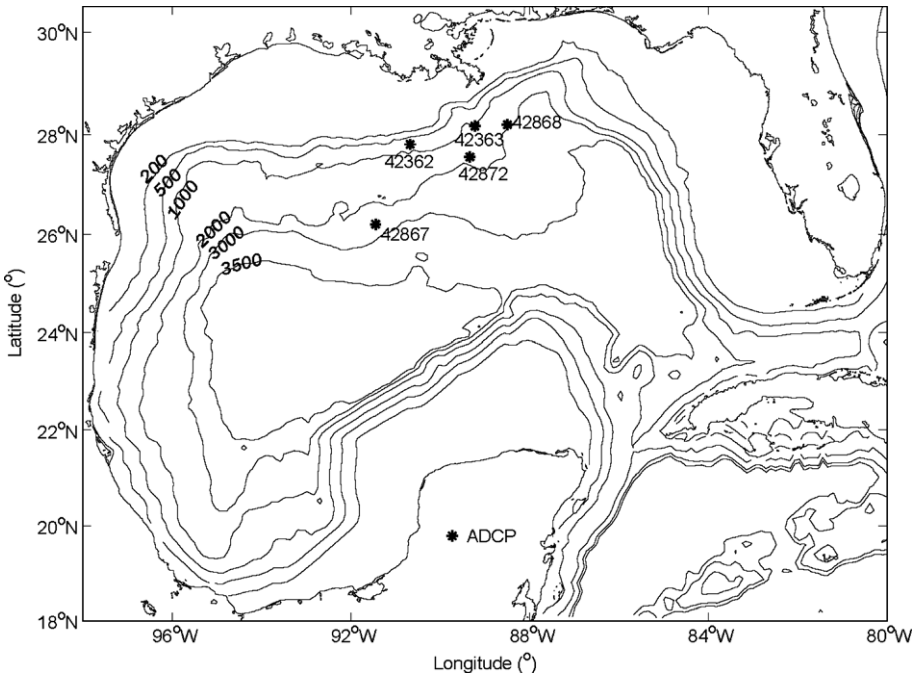

Fig. 6. ADCP stations where model results are compared against observed currents. Contours are isobaths in meters.

4.1. Comparison against satellite SSH

When comparing the model results against satellite SSH, one should be mindful that the latter is not the "truth." In addition to uncertainty in the mean, satellite maps are based on objective analyses with presumed spatial and temporal scales (Ducet et al., 2000). In some cases, the model can provide more accurate information pertaining to the small and fast scales of the real ocean (Wang et al., 2003; Oey et al., in press). Nevertheless, satellite data are suited for studying larger-scale eddies and Loop Current which are the focus of this work (e.g., Leben, 2005).

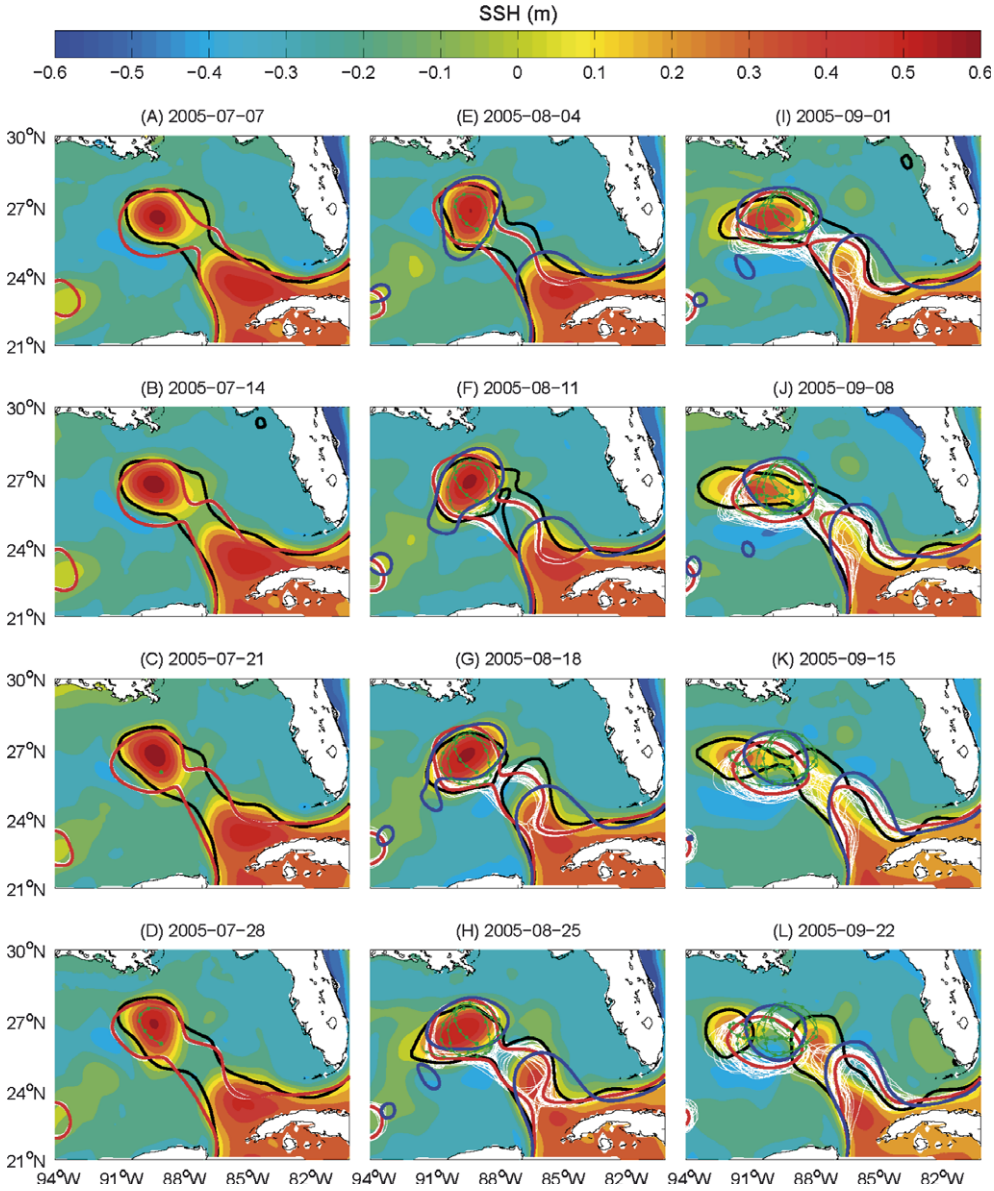

Fig. 7. Daily averaged SSH's shown weekly during the last 4 weeks of breeding (A–D) and 8 weeks of forecast (E–L). Background color is ConA. Lines are SSH = 0 contours of: black: AVISOM; red: EnMB's (A–D) and EnMF's (E–L); white: EnB members (A–D) or BEnF members (E–L); and blue: ConF. Green line is drifter trajectory marked daily, shown from Jul/21. See Appendix 1 for acronyms.

Fig. 7 shows daily averaged SSH plotted every week from *Jul/07* through *Sep/22/2005*. The background color is ConA. The SSH = 0 lines are plotted for satellite (i.e. *AVISO*+ ten-year model mean, henceforth AVISOM; black), ConF (blue), ensemble mean (red) and ensemble members (white); the contour lines give in each case the corresponding estimates of the frontal positions of the Loop Current and rings. The track of a surface drifter is shown in green beginning at *Jul/21*. In this case, the breeding ends and hence forecasts start on *Jul/28/2005*; the last four weeks of the *8-week* breeding (Fig. 7A–D) and the entire *8-week* forecast (Fig. 7E–L) are shown. The ConA can be seen to be similar to *AVISOM*, though the former shows a warm ring that is nearly or already detached throughout the period shown in Fig. 7, whereas the Loop Current in AVISOM maps appear to be on the verge of shedding a ring (e.g., Fig. 7F and G), but did not do so until *Sep*/15–22 (Fig. 7K and L). On the other hand, the ensemble mean agrees well with AVISOM throughout the breeding period (EnMB; through *Jul/28*, Fig. 7A–D), and also for the first five weeks of the forecast (EnMF; *Jul/28–Sep/01*, Fig. 7E–I). After *Sep/01*, the Loop current rapidly extends westward in an elongated shape (Fig. 7I and J). Thereafter a warm ring is shed (Fig. 7K–L), and both ConF and EnMF fail to reproduce AVISOM or the ConA. When interpreting satellite SSH, there is some uncertainty with regard to the mean. We have therefore checked the AVISOM maps against (1) SSH maps using the original *AVISO* mean estimated from a seven-year altimetric mean SSH, (2) the University of Colorado's (UOC) maps(http://argo.colorado.edu/~realtime/gsfcgom-real-time_ssh/) and (3) the NOAA/AOML maps (http://www.aoml.noaa.gov/phod/dataphod/work/trinanes/INTERFACE/index.html) using different model means. These various maps yield similar results. Most of the differences occur during the first 8–9 weeks (*Jul/07–Sep/01*) shown in Fig. 7. During that period, the NOAA/AOML and AVISO maps show a Loop Current-ring system that is either disconnected or barely connected – features that are in between AVISOM (more connected) and the ConA (less connected) maps of Fig. 7, whereas in UOC maps the Loop-ring system is more smoothly connected.

During and a few days after the passage of a hurricane, the ocean surface undergoes rapid temporal and spatial changes that cannot be accurately depicted by maps such as the AVISOM (Oey et al., in press). Nonetheless, *AVISO* (or other similar products) provides a yardstick to check forecast results before and (days) after the hurricane. Fig. 7 suggests that the EnMF (red) is visually better than the ConF (blue). A more quantitative assessment is shown in Fig. 8 which plots the correlations between various modeled and *AVISO SSHA*'s (upper panel) over the region north of 23 °N and west of 84 °W, and where the water depths $\geqslant$500 m. The corresponding RMS differences ("errors"; lower panel) are also shown. The figure shows that ConA for the entire period, EnMB for the first 8 weeks and EnMF during the first 4–5 weeks of the forecast period all have relatively high correlations and small RMS errors. The ConA-*AVISO* correlation is approximately 0.9 during the first *6 weeks*, and decreases to about 0.74 at the 9–11th weeks before increasing again to approximately 0.85 at the end of the forecast period, a max–min range of about 0.16. At the beginning date of the forecast, *Jul/28*, the EnMB has a slightly higher correlation (about 0.05) and a lower RMS error (about 0.02 m) than the ConA. But these differences are small and statistically insignificant. Lin et al. (in press) analyzed the 1999–2000 satellite data and found that the ConA-*AVISO* correlation can fluctuate from low's of about 0.67 to high's of 0.9 within a 1–3-month period when the Loop Current and rings undergo rapid changes: as for example when a ring separates from the Loop Current, or when the Loop Current retracts or expands (e.g., Oey et al., 2003). The standard deviation for the period 1999–2000 is 0.18. Their results are consistent with the variation of ConA-*AVISO* correlation shown in Fig. 8.

Fluctuations in ConA-*AVISO* correlation (and in the corresponding RMS error) reflect the fact that both the satellite SSHA maps and model have errors which are most pronounced during periods of large changes in the Loop Current and rings; this is indeed the case during the present study period (see Fig. 7). The above-mentioned differences between EnMB and ConA at the initial forecast date (*Jul/28*), or indeed the differences between EnMB, ConA and EnMF during the first 12–13 weeks of the study period in Fig. 8, are therefore statistically insignificant when compared with the variability of the errors inherent in the satellite SSHA maps and model. It is therefore significant that EnMF provides a good forecast through the time when *Katrina* arrived (*Aug/25*). In comparison, the quality of ConF deteriorates after only 1–2 weeks of forecast (*Jul/28–Aug/11*, Fig. 8). The EnMF (and BEnF members) deteriorates after *Katrina*, in the final 2–3 weeks of forecast. It will be an interesting future research to study if the rapid decline in the forecast quality in these final weeks is dynamically related to the intense disturbances caused by the hurricane.

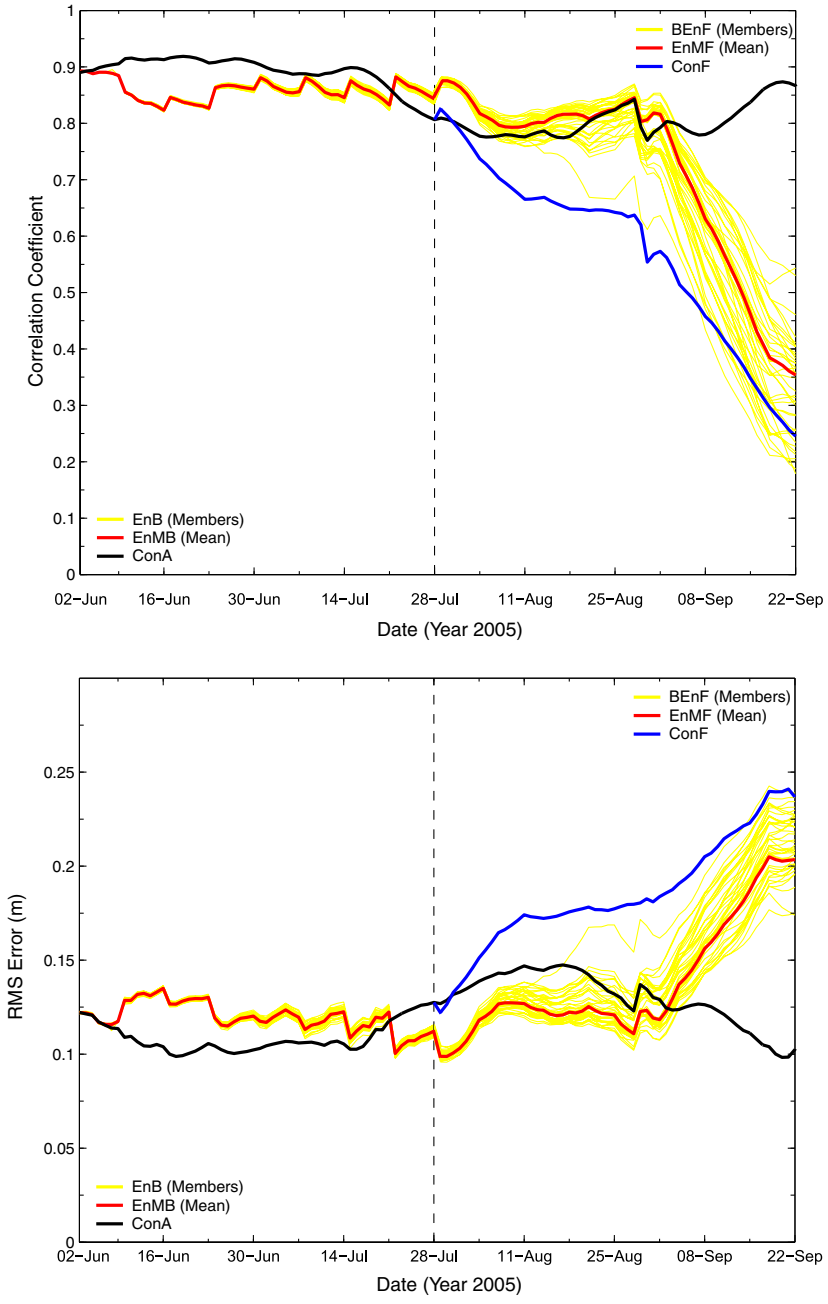

Fig. 8. Upper panel: correlation between AVISOM and various model SSHA's as indicated for the region north of 23 °N, west of 84 °W and in water with depths >500 m; lower panel: the corresponding root mean squared SSHA error. Vertical dashed line indicates the initial date of forecasts. See Appendix 1 for acronyms.

To ascertain that the above findings (that EnMF gives superior forecasts to the ConF) hold for different periods, we conducted ten additional forecast experiments, i.e. ten different samples of initial ocean states. The forecast start-dates of seven of these are successively weekly shifted from that shown in Fig. 8; they produce similar results as Fig. 8 (not shown). The three others are more interesting as the start-dates: *Nov/01/2005*, *Mar/18/2006* and *Aug/25/2006*, are more widely separated, by 3–4 months. The corresponding correlations and RMS errors are shown in Fig. 9. The EnMF can be seen to consistently outperform ConF even for the worse breeding case

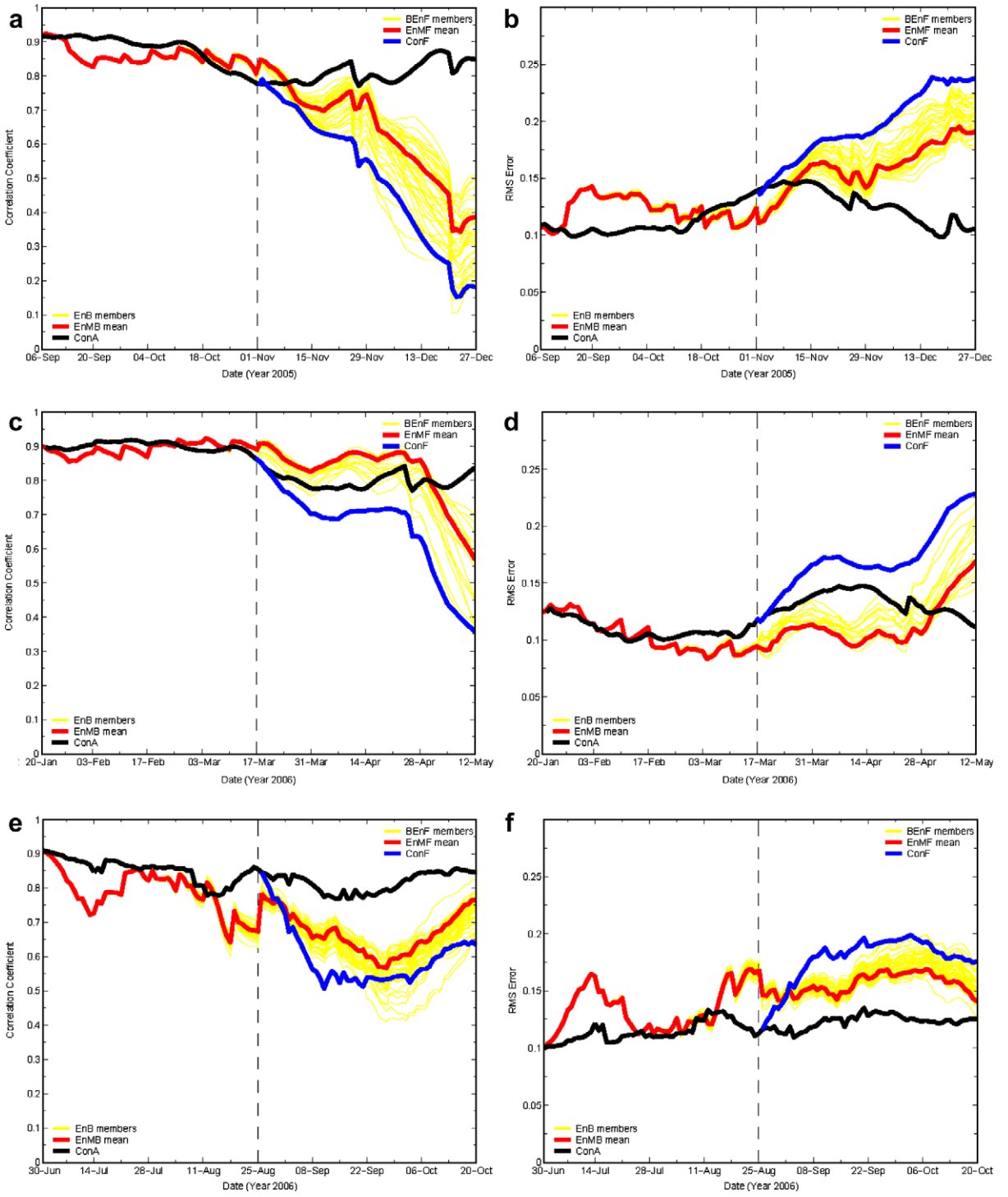

Fig. 9. Correlation between AVISOM and model SSHA's (left panels A, C and E) and the corresponding root mean squared SSHA errors (right panels B, D and F), as in Fig. 8, for three different forecast start dates: *2005/Nov/01* (A & B), *2006/Mar/17* (C & D), and *2006/Aug/25* (E & F).

of Fig. 9E and F. These findings are consistent with Leith's (1974) theoretical analysis, mentioned previously. Figs. 8 and 9 show that useful forecasts of mesoscale eddies may be obtained for up to 4–6 weeks.

4.2. Comparison against NOAA drifter

We compare paths of modeled drifters with the trajectory of the *NOAA* drifter shown in Fig. 7 for an eight-week period from *Jul/21* through *Sep/15*, as follows (cf. Fan et al., 2004). For each of the eight 7-day periods, a (model) drifter is released at the "*day-0*" position of the observed drifter, and is tracked for 7 days using Awaji et al.'s (1980) method. This gives eight sample trajectories and the corresponding deviation distances (i.e. errors) which are then averaged. Fig. 10 plots averaged deviations for ConA, EnMF, AVISOM and ConF, and Fig. 11 the trajectories. All four cases are similar in the first 2–3 release days, with errors for ConA and AVISOM slightly less than EnMF or ConF. At *day-7*, ConA produces the least error (as can be expected) while EnMF gives an improved forecast than ConF (and AVISOM). These improvements can be seen in Fig. 11. The EnMF (red with markers) trajectories generally follow the observed (magenta with markers) trajectories from the week-1 forecast (Fig. 11A) through the period of *Katrina* (Fig. 11F); the EnMF trajectories deviate from the observed during the 7–8th *weeks* of the forecast (Fig. 11G and H). In contrast, the ConF trajectories begin to deviate from the observed in the 4th *week* (Fig. 11D).

4.3. Comparison against ADCP observations

Five ADCP time series over the northern Gulf of Mexico were available during the forecast period *Jul/21–Sep/15/2005* (Fig. 6 shows the ADCP locations). These ADCP's were operated by the oil industry; through an arrangement with MMS and NOAA the data were made publicly available at the NDBC site http://www.ndbc.noaa.gov/. All five ADCP's returned velocity data through *Aug/27/2005* just before *Katrina* arrived at the northern Gulf, from approximately −75 m through −1000 m at depth intervals of about 30 m. Three ADCP's (42868, 872 and 867) intermittently returned data after the storm (see Fig. 12). The data were processed for obviously bad values (either discarded or linearly interpolated from neighboring good values if the gap is less than 1 day), and daily averaged. The modeled velocities were also daily averaged and interpolated onto the observation locations. Fig. 12 compares the observed and forecast (EnMF and ConF) speeds as a function of time and depth.

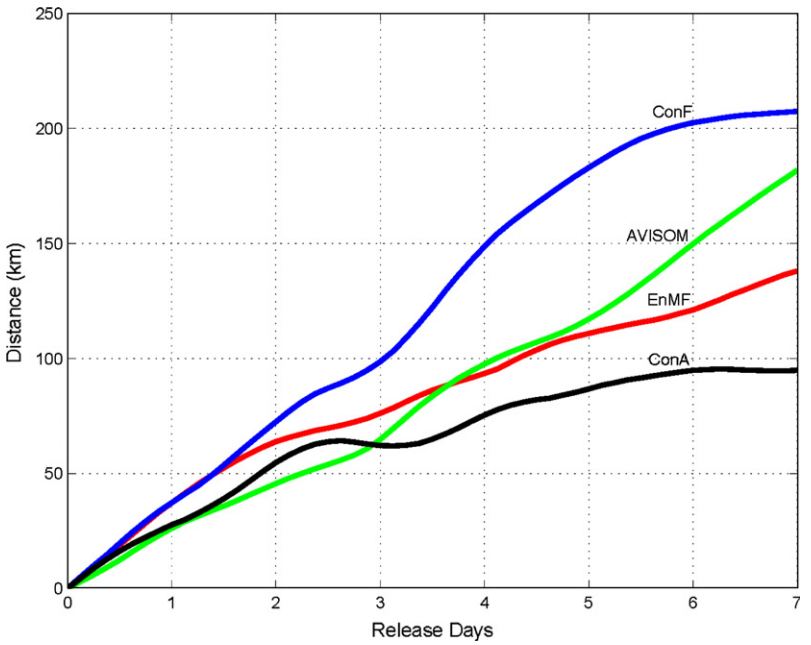

Fig. 10. Averaged deviations of the indicated model drifter trajectories from the observed trajectory as distances in km, plotted as a function of drifter release-days. The averaging is over the eight 7-day periods (or ensembles) from Jul/21 through Sep/15/2005. See Appendix 1 for acronyms.

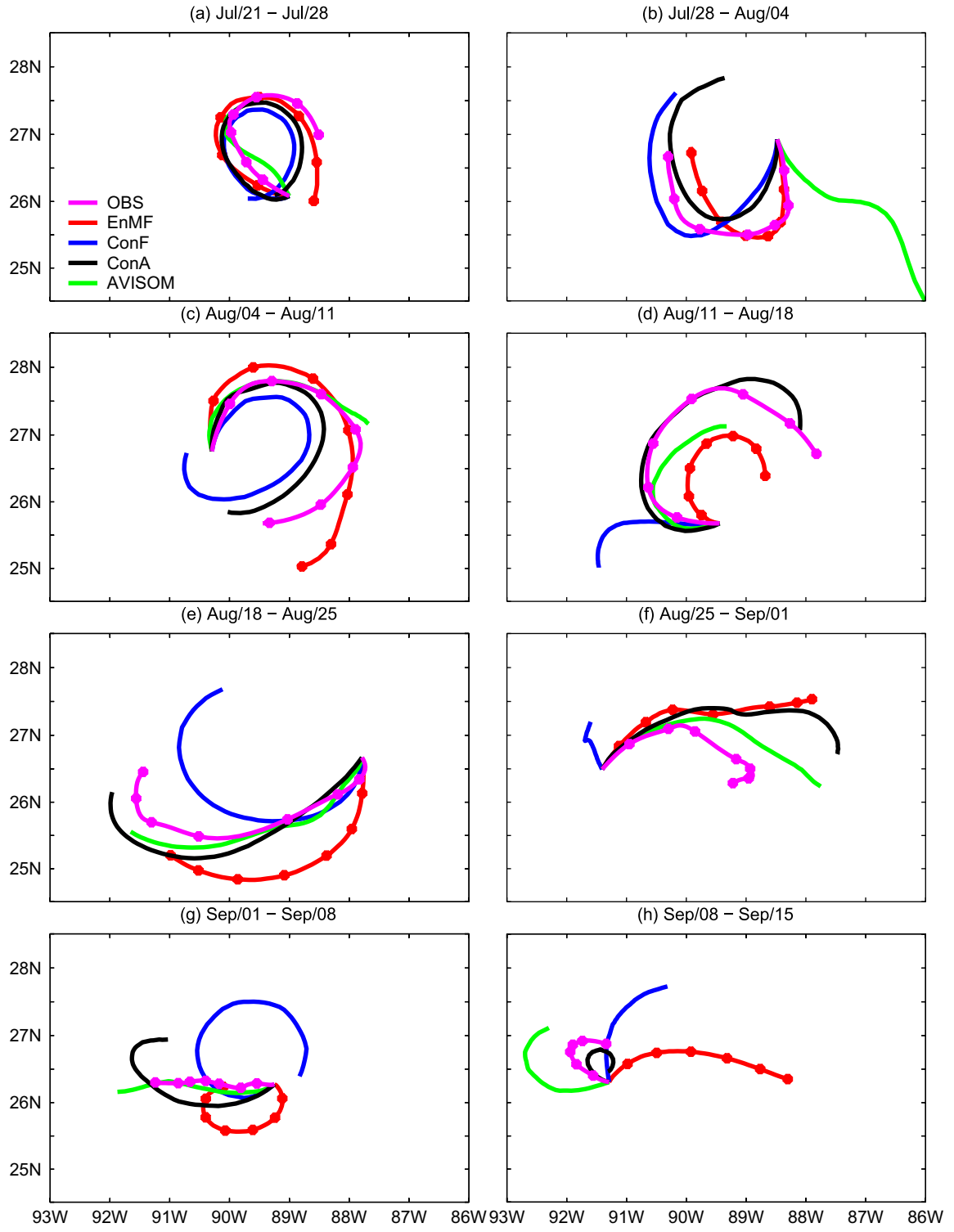

Fig. 11. Modeled and observed drifter trajectories for each of the eight release periods from Jul/21 through Sep/15/2005. Markers on "OBS" and "EnMF" indicate the daily positions. See Appendix 1 for acronyms.

Because of their locations, the ADCP's measured currents around the western, northwestern and northern rims of the Loop-ring system (cf. Fig. 7). In the upper 400 m, directions are predominantly northward, northeastward and eastward. Fig. 12 shows observed speeds $> \approx 1$ m/s at the three northeastern stations "868," "363" and "872" (Figs. 12a–12c) closest to the Loop-ring system. At the first two stations, speeds reached a maximum around *Aug/11*, after which date the Loop-ring system began to move west-southwestward away from the moorings; at "872" currents remained strong through *Aug/27*. At the northwestern station "362" (Fig. 12d), currents were moderately strong (0.5–0.6 m/s) at the beginning, *Jul/21–Aug/04*, but diminished thereafter as the Loop-ring system drifted southward. At the southwestern station "867" (Fig. 12e), speeds did not become strong until later, around *Aug/11–18*, and also in September. The forecasts, the EnMF in particular, reproduce these gross observed features. The error plots in the lower two panels of Figs. 12a–12e show

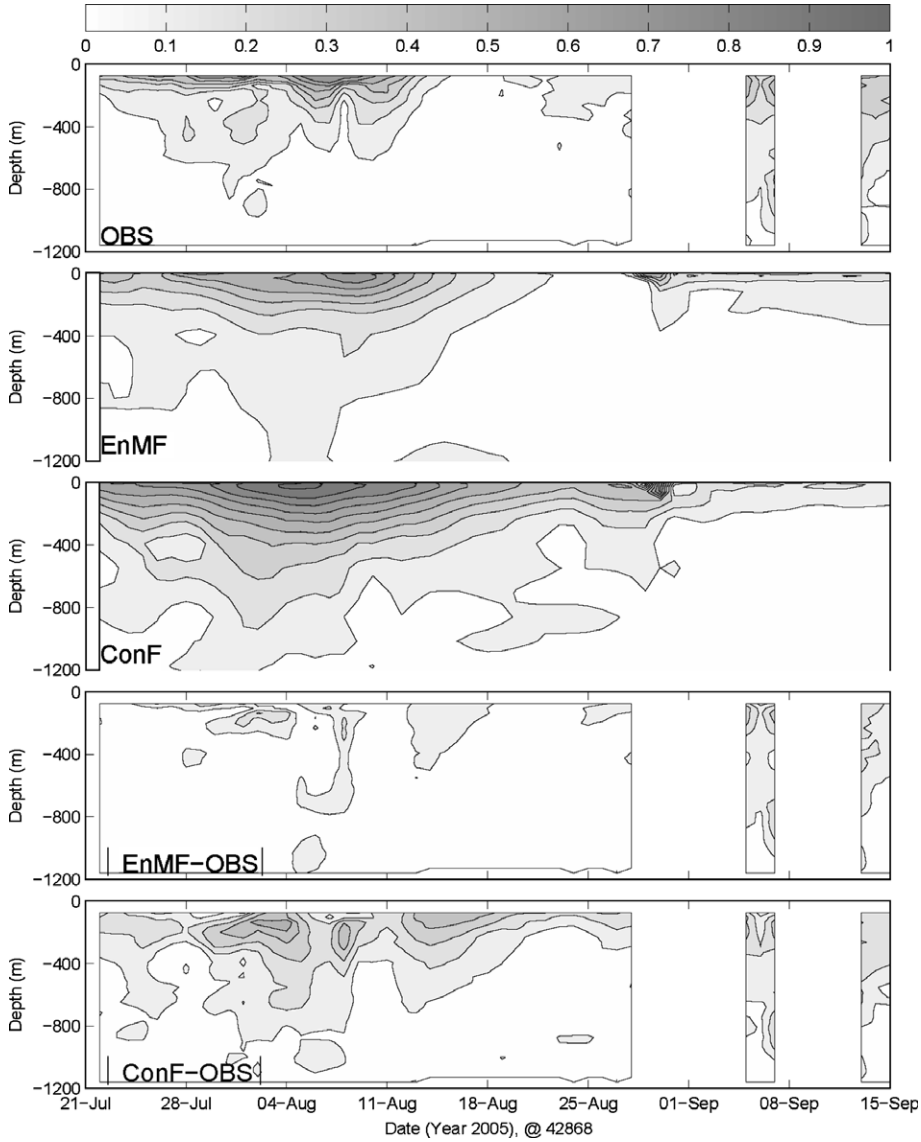

Fig. 12a. Comparisons between modeled and observed speeds (m/s) at ADCP station 42868 for the period Jul/21 through Sep/15/2005. From top to bottom panels: observation, EnMF, ConF, |EnMF-Obs| and |ConF-Obs|. See Fig. 6 for ADCP locations, and Appendix 1 for acronyms.

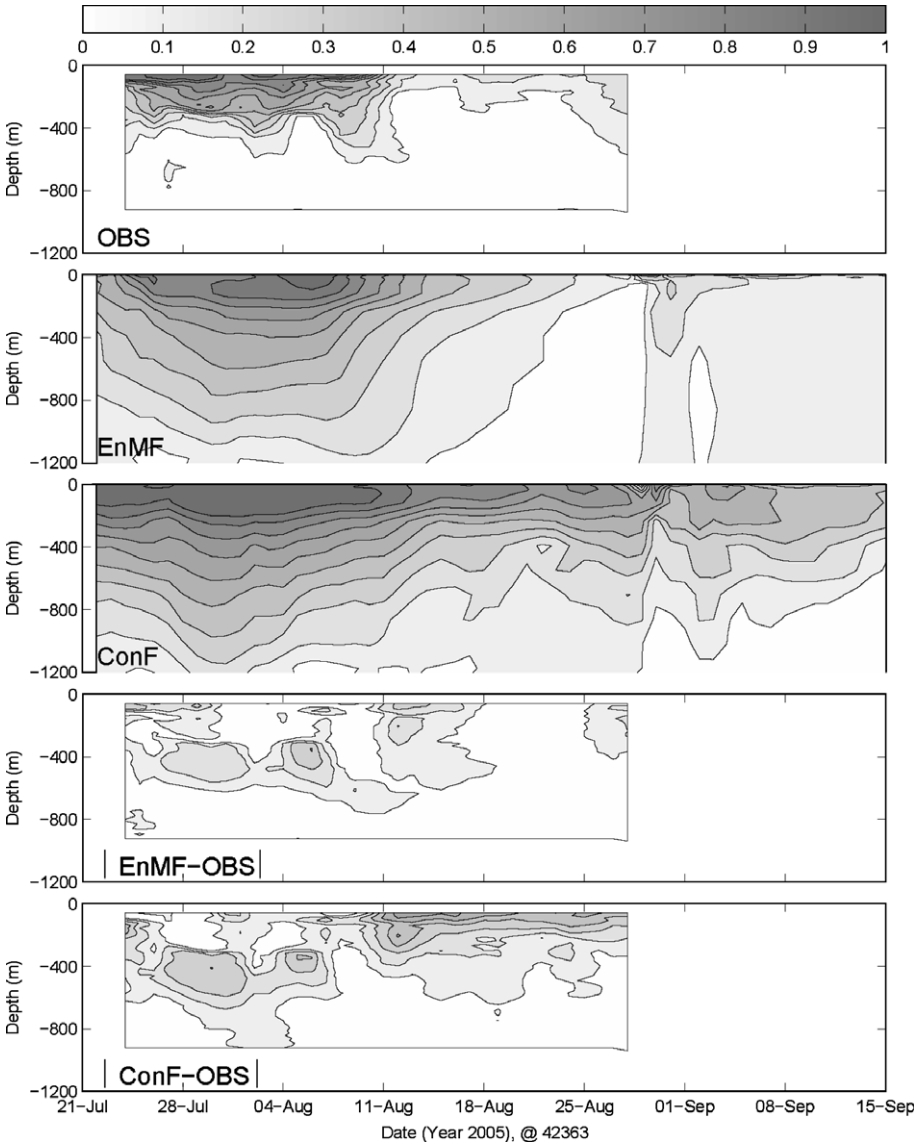

Fig. 12b. Same as Fig. 12a at ADCP station 42363.

that the EnMF generally gives a more accurate depiction of the observed speeds than the ConF. However, forecast vertical shears are weaker than those observed (e.g., stations "868" and "363," Figs. 12a and 12b).

Additional measures of the forecast skill are given in Fig. 13. In Fig. 13a we show the complex correlations (CC's) computed in time as a function of depth, and in Fig. 13b the complex correlations were computed in the vertical as a function of time (Kundu, 1976; see Appendix 2). Correlation amplitude $|CC| \approx 1$ and phase $\theta_{CC} \approx 0$ would indicate that the modeled and observed currents match closely in time (Fig. 13a; temporal CC) or in the vertical (Fig. 13b; vertical CC). The temporal CC's for EnMF are clearly improved over those for ConF at all stations except "872" where both show comparable values. The CC's (for EnMF) are high $> \approx 0.8$ near the surface $z > \approx -200$ m at all stations except "867" where $|CC| \approx 0.5$ and $|\theta_{CC}| \approx < 15°$ for $z > \approx -400$ m. In particular, at station "362," $|CC| \approx 0.9$ and $|\theta_{CC}| \approx < 15°$ throughout the water column. As plots for the individual EnF members in Fig. 13 show, there is greater uncertainty (spread) in the forecast results deeper in the water column. The improvement in EnMF over ConF is less clear for vertical CC's (Fig. 13b). This is because both forecasts are in general less correlated with observations at deeper levels

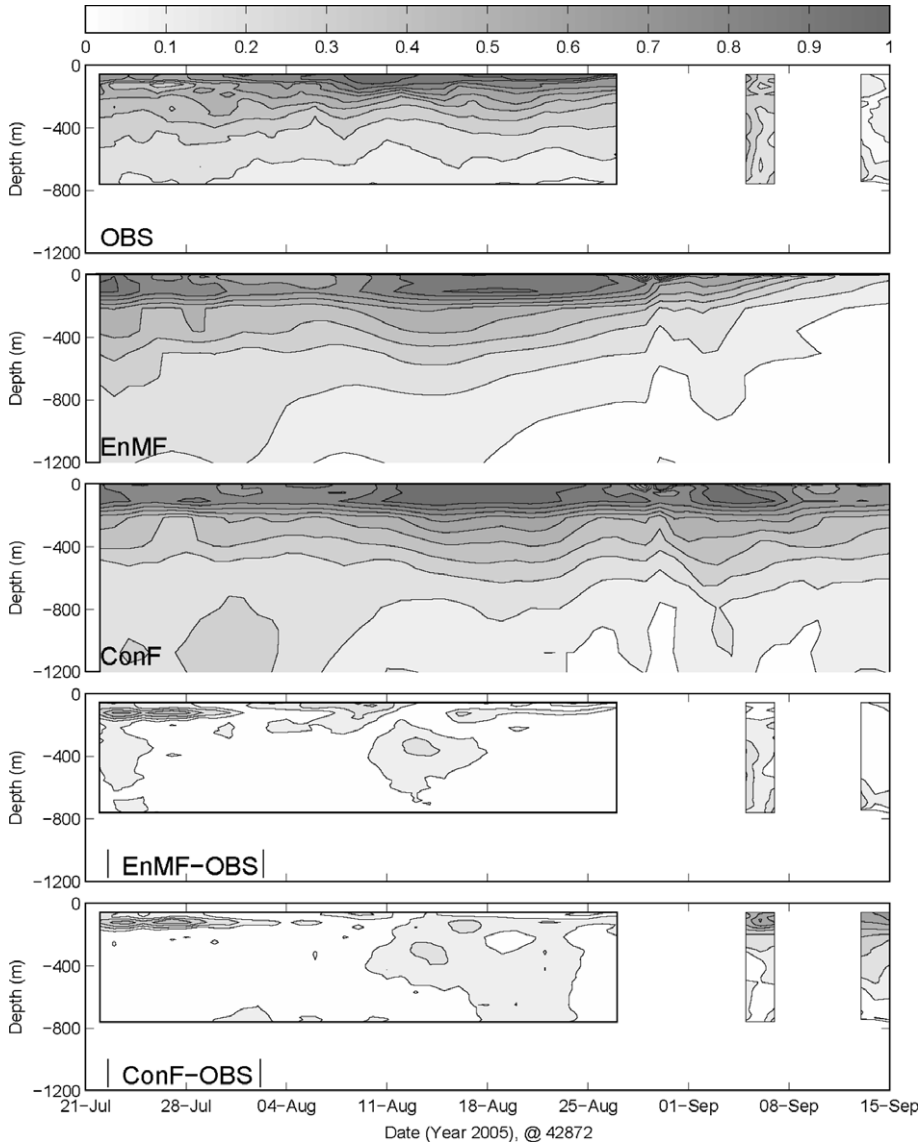

Fig. 12c. Same as Fig. 12a at ADCP station 42872.

(cf. Fig. 13a). Fig. 13b shows that both forecasts have comparable CC-values. One can identify periods when $|CC| > \approx 0.7$ and $|\theta_{CC}| \approx < 25°$ at stations "868" and "363" prior to *Aug*/18, station "872" between *Aug*/11–27 and also *Sep*/3–6, station "362" prior to *Aug*/*4* and station "867" from *Aug*/14–25 and also around *Sep*/15. Forecast uncertainty in general increases with time at all stations except for the southwestern-most station "867," where the model appears to show a more consistent prediction (less spread) as the approach of the Loop-ring system at later forecast dates (*Aug*/14–25 and also around *Sep*/15).

5. Conclusions

This paper uses the bred-ensemble forecast (BEnF) technique (Toth and Kalnay, 1993; Toth and Kalnay, 1997) to estimate the locations and strengths of the Loop Current and ring in *Jul–Sep*/*2005*, a period during which hurricane *Katrina* (*Aug*/*24–30*) passed over the eastern and northeastern Gulf of Mexico. We show that breeding (after 7–8 cycles) produces growing modes (bred vectors) which have patterns and growth rates akin

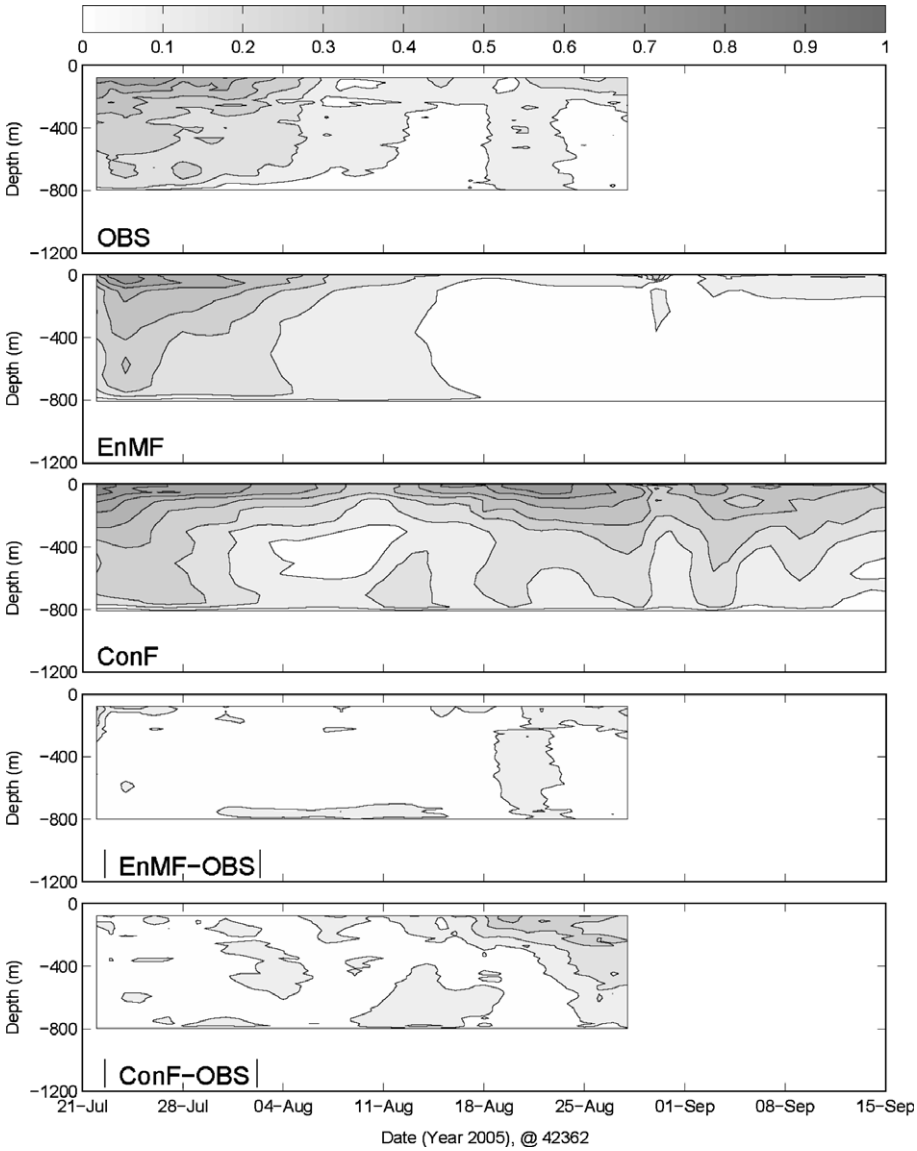

Fig. 12d. Same as Fig. 12a at ADCP station 42362.

to baroclinic unstable modes in the Gulf of Mexico, with largest amplitudes in the vicinity of the Loop Current and ring. The bred vectors represent the uncertainty in our analysis (initial state). Previous atmospheric experiences indicate that the use of these bred vectors as perturbations in ensemble forecasting can improve the forecast.

To assess model skills, results from the control analysis (ConA), control forecast (ConF), and ensemble mean forecast (EnMF) are compared against observations consisting of satellite, drifter and ADCP data. The EnMF is found to be statistically indistinguishable from ConA for the first 4–5 *weeks* of the forecast. This is a rather surprising result though it needs to be confirmed in future studies with a large sample of forecast cases and with different models. We show that EnMF consistently produces superior forecasts to the ConF, in that the EnMF results are "closer" to the observations. Ensemble forecasting is also useful in that by examining the forecast-spread (of the Loop Current frontal positions for example) of the ensemble members, one can estimate the reliability of the forecast (it is a questionable forecast if there is too much

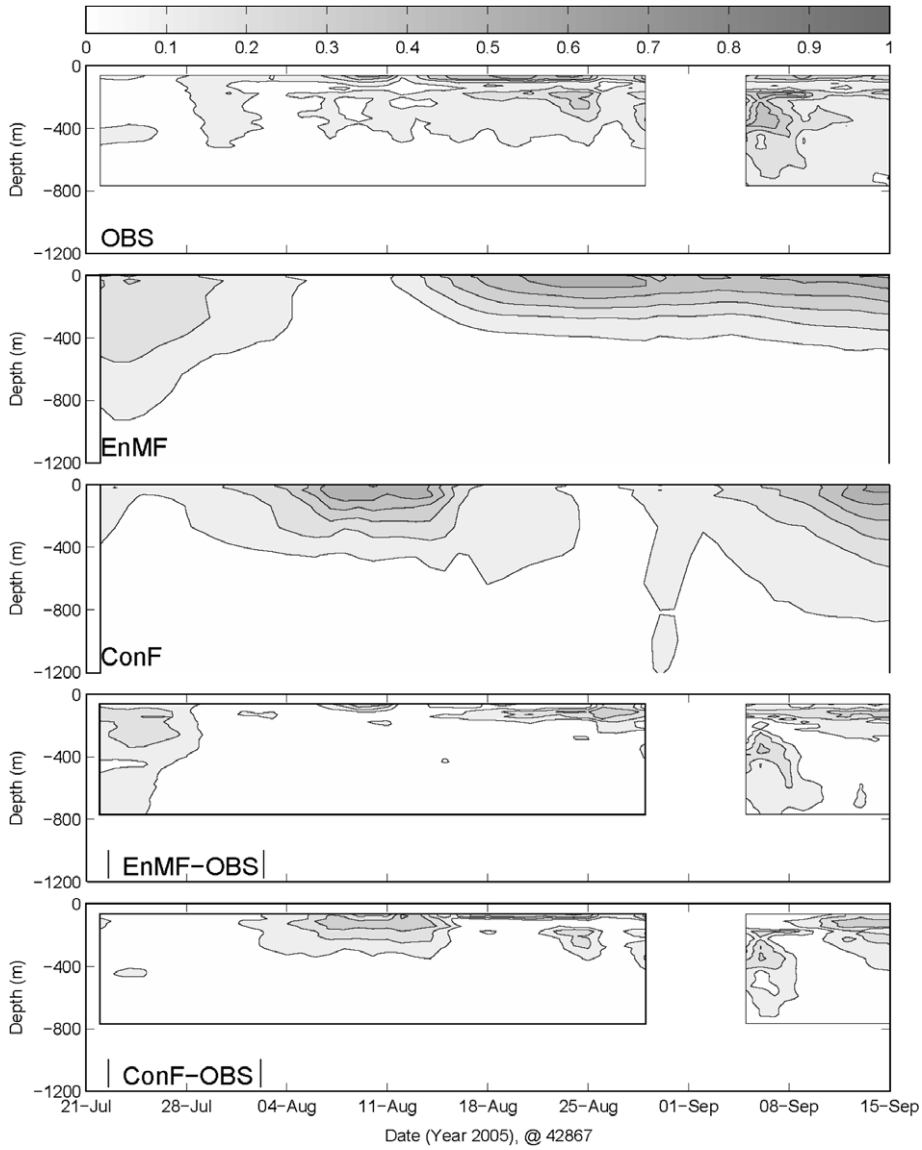

Fig. 12e. Same as Fig. 12a at ADCP station 42867.

spread; cf. Figs. 7E–H with I–L; also Fig. 13a, stations 42872 and 867), as well as the forecast probability (for cases in which members are clustered in 2 or 3 distinct groups).

The implications of our results for future work follow. Firstly, the EnMF provides a viable way to more accurately estimate ocean responses to hurricanes. This is because these responses are rapid and locally intense, and data assimilation using smoothed satellite SSHA maps in ConA can produce false results (cf. Oey et al., 2006; Oey et al., in press); good BEnF during the first 4–5 *weeks* before the storm can provide a better alternative. Secondly, for the same reason, EnMF should provide a more accurate ocean field (which is input to wave models such as the WaveWatch-3 model or the Simulating WAves Nearshore – SWAN model) for estimating surface waves. Thirdly, the EnMF provides an alternative means by which one can more accurately estimate the locations and strengths of oceanic warm features (Loop Current and rings), which in turn may aid in hurricane predictions (DeMaria et al., 2005). Finally, bred vectors may be used to provide time-dependent error covariance to improve analyses.

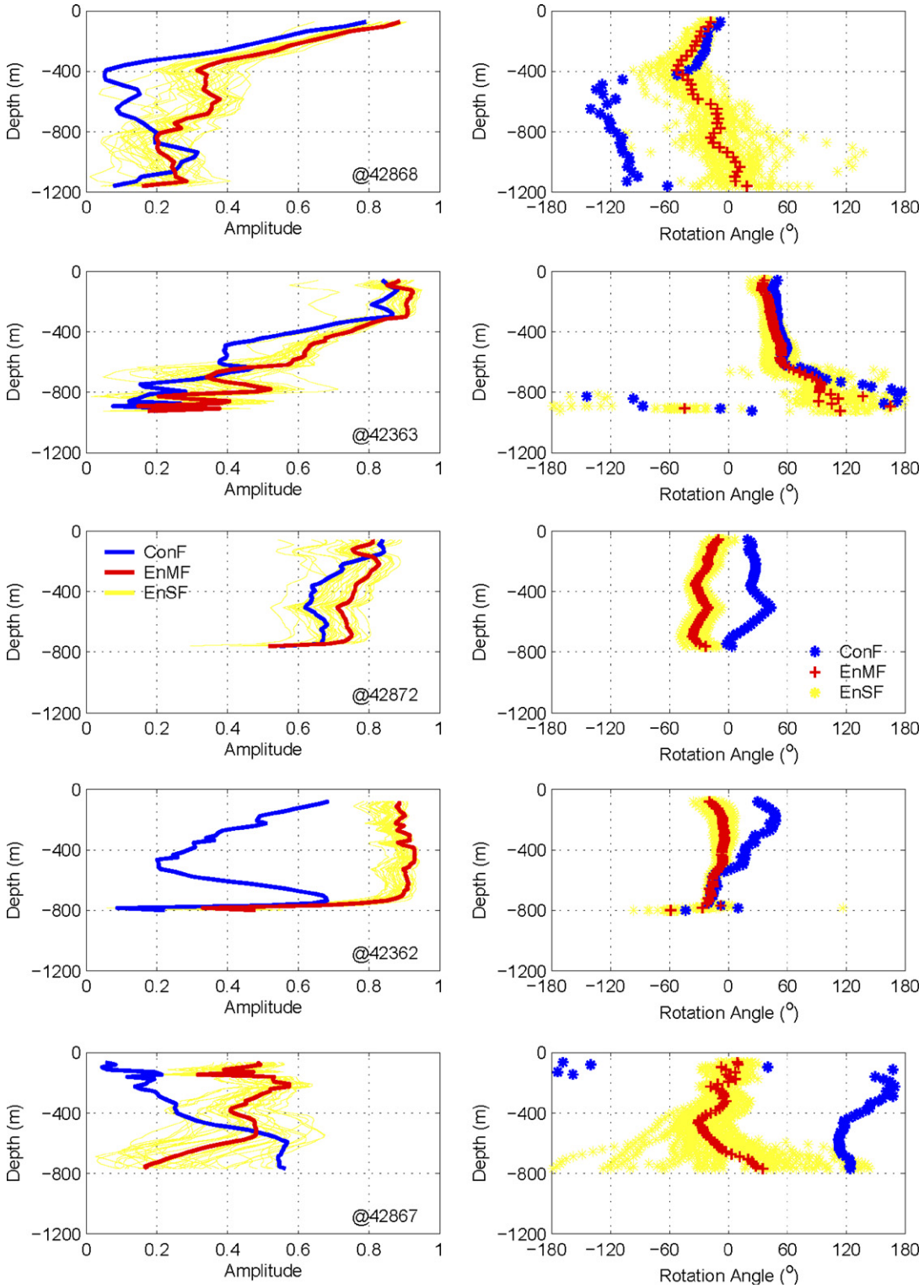

Fig. 13a. Vector correlations of currents at the five ADCP stations with EnMF (red) and also with ConF (blue): left column is the amplitude and right column is rotation angle (positive means model is rotated anticlockwise from observation). At each station, the correlations are computed over the time period from Jul/21 through Sep/15/2005, then plotted as a function of depth. See Appendix 1 for acronyms. (For interpretation of the references in colour in this figure legend, the reader is referred to the web version of this article.)

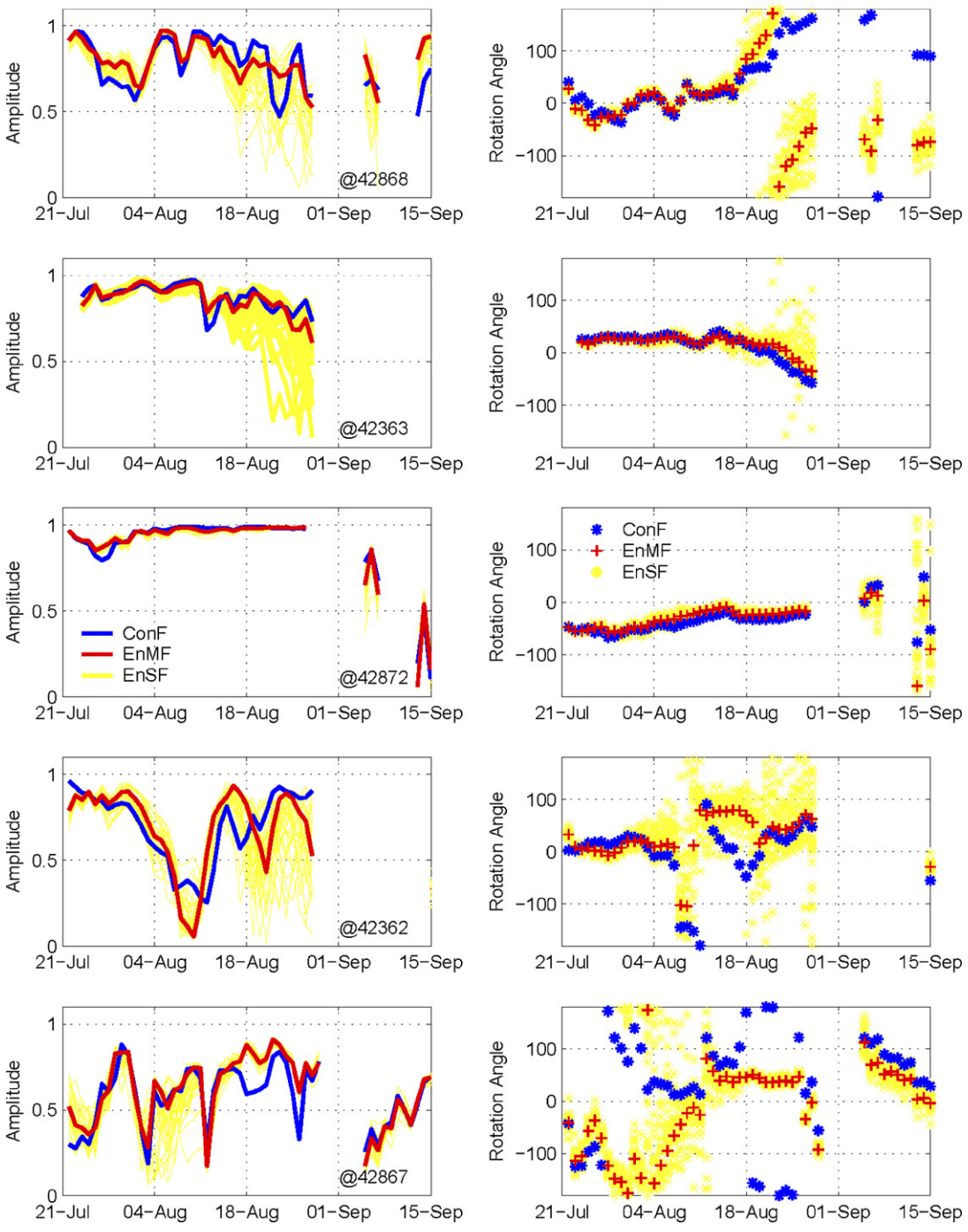

Fig. 13b. Same as Fig. 13a, but now the vector correlations are computed over the water column (-100 m $\gtrapprox z \gtrapprox -1000$ m), then plotted as a function of time from Jul/21 through Sep/15/2005. See Appendix 1 for acronyms.

Acknowledgement

We are grateful to the Minerals Management Service (MMS) for supports (Contract #1435-01-06-CT-39731). We profit immensely from Professor Kalnay's and Dr. Yang's seminars at Princeton on bred-ensemble techniques. Comments from Prof. George Mellor and two anonymous reviewers improve the manuscript.

Encouragements from Drs. Carole Current, Walter Johnson and other colleagues during the course of the research are appreciated. Computing was conducted at GFDL/NOAA.

Appendix 1. Acronyms and definitions of some variables

Acronym Meaning

ADCP Acoustic Doppler Current Profiler
AOML Atlantic Oceanographic and Meteorological Laboratory
AVISO Archiving, Validation and Interpretation of Satellite Oceanographic data
AVISOM AVISO SSHA+ the (present) model 10-year mean SSH
BEnF Bred Ensemble Forecast
ConA Control analysis; sometimes referred to as hindcast or nowcast in the literature and is often used as initial field for forecasting
ConF Control Forecast, meaning the "conventional" (single) forecast
EnB Ensemble breeding
EnMB Ensemble mean breeding
EnMF Ensemble mean forecast
GCM General Circulation Model
GODAE Global Ocean Data Assimilation Experiment
HRD Hurricane Research Division
NCEP National Centers for Environmental Prediction
NOAA National Oceanic & Atmospheric Administration
OBS Observation(s)
OHC Ocean Heat Content
POM Princeton ocean Model
RMS Root Mean Square
SSH Sea Surface Height
SSHA Sea Surface Height Anomaly
SST Sea Surface Temperature

Variable Meaning

$\varepsilon_m\,(kN)$ perturbation of the mth member of a breeding cycle, $k = 0, 1, \ldots, K$; the last one for $k = K$ is used (with the corresponding control analysis) to initialize the ensemble forecasts – see $T_m\,(kN)$ definition below
$\delta\eta$ sea surface height anomaly or SSHA
$\delta\eta_0$ observed sea surface height anomaly from satellite
$\delta\eta^f(n)$ unperturbed (i.e. conventional) forecast SSHA(i.e. ConF) at time "n"
$\delta\eta^f_m(n)$ perturbed mth-member forecast SSHA at time "n"
$A_m(n)$ spatial average of the mth-member bred vector at time "n"
$\boldsymbol{BV}$ bred vector = the difference between perturbed and unperturbed forecasts
CC complex correlation between two vectors, also called vector correlation
GR_k bred-vector growth rate for the kth-cycle
K total number of breeding cycles; this paper has used $K = 8$ and 10
M total number of ensemble members; this paper uses $M = 20$
N number of days *per* breeding cycle; this papers uses $N = 7$
T potential temperature; also used more generally to denote a state vector
$T_m\,(kN)$ mth ensemble member of the perturbed analysis of "T" at the start of a breeding cycle, i.e., $T_m(kN)=T^a(kN) + \varepsilon_m(kN)$, $k = 0, 1, \ldots, K-1$. For $k = K$, $T_m(KN)$ is used to initialize the ensemble forecasts
T^a "T" obtained from a control analysis or ConA
$T^f(n)$ unperturbed (i.e. conventional) forecast (i.e. ConF) at time "n"
$T^f_m(n)$ mth-member of the perturbed forecast at time "n"

Appendix 2. Complex correlation (CC)

The "CC" between two velocity time series $\mathbf{u}_1 = (u_1, v_1)$ and $\mathbf{u}_2 = (u_2, v_2)$, is defined as (Kundu, 1976):

$$\mathrm{CC} = \langle w_1 w_2^* \rangle / [\langle w_1 w_1^* \rangle^{1/2} \langle w_2 w_2^* \rangle^{1/2}], \tag{A1}$$

where $w_n = u_n + \mathrm{i}v_n$, $n = 1, 2$, $\mathrm{i} = (-1)^{1/2}$, the asterisk indicates the complex conjugate, and $\langle \cdot \rangle$ denotes time averaging. Kundu (1976) was interested in the veering angle between $\mathbf{u}_1$ and $\mathbf{u}_2$ in the bottom Ekman layer and showed that the phase of CC, θ_{CC}, is the average veering angle (between the two vectors) weighted by the speeds of the instantaneous vectors. For the present case, CC measures how closely the model vector w_1 follows the observation vector w_2 in their indexed space, which can be the spatial dimension (e.g., in the vertical at a given time) or time as in ADCP time series at a fixed depth. Clearly, θ_{CC} should be small for the two vectors to be 'close,' but |CC| should also be ≈ 1 (|CC| is <1 from (A1)). By considering simple sinusoids, it can be shown that |CC| is small if $\mathbf{u}_1$ and $\mathbf{u}_2$ have disparate frequencies. For similar frequencies $|\mathrm{CC}| \approx \cos(\phi)$, where ϕ is the (average) phase-shift between $\mathbf{u}_1$ and $\mathbf{u}_2$. On the other hand, θ_{CC} is independent of ϕ, so that it is possible for $|\mathrm{CC}| = 1$ but $\theta_{CC} = 90°$, and vice versa for $|\mathrm{CC}| = 0$ but $\theta_{CC} = 0$. The behavior of CC is more complicated for general time series. The upshot is, for the model analysis to be any good, we require $|\mathrm{CC}| \approx 1$ and $\theta_{CC} \approx 0$.

References

Anderson, D.L.T., Sheinbaum, J., Haines, K., 1996. Data assimilation in ocean models. Rep. Prog. Phys. 59, 1209–1266.

Awaji, T., Imasato, N., Kunishi, H., 1980. Tidal exchange through a strait: a numerical experiment using a simple model basin. J. Phys. Oceanogr. 10, 1499–1508.

Bye, J.A.T., Jenkins, A.D., 2006. Drag coefficient reduction at very high wind speeds J. Geophys. Res. 111 (C3), C03024. doi:10.1029/2005JC003114.

Caplan, P., Derber, J., Gemmill, W., Hong, S.-Y., Pan, H.-L., Parrish, D., 1997. Changes to the NCEP operational medium-range forecast model analysis/forecast system. Wea. Forecast. 12, 581–594.

Cochrane, J.D., 1972. Separation of an anticyclone and subsequent developments in the Loop Current (1969). In: Capurro, L.R.A., Reid, J.L. (Eds.), . In: Texas A&M Univ. Ocean Studies, vol. 2. Gulf Publishing Co, Houston, pp. 1–106.

Cooper, C., Forristall, G.Z., Joyce, T.M., 1990. Velocity and hydrographic structure of two Gulf of Mexico warm-core rings. J. Geophys. Res. 95, 1663–1679.

Craig, P.D., Banner, M.L., 1994. Modeling wave-enhanced turbulence in the ocean surface layer. J. Phys. Oceanogr. 24, 2546–2559.

DeMaria, M., Kaplan, J., 1994. Sea surface temperature and the maximum intensity of Atlantic tropical cyclones. J. Climate 7, 1324–1334.

DeMaria, M., Mainelli, M., Shay, L.K., Knaff, J.A., Kaplan, J., 2005. Further Improvement to the Statistical Hurricane Intensity Prediction Scheme (SHIPS). Wea. Forecast. 20, 531.

Donelan, M.A., Haus, B.K., Reul, N., et al., 2004. On the limiting aerodynamic roughness of the ocean in very strong winds. Geophys. Res. Lett. 31, L18306. doi:10.1029/2004GL019460.

Ducet, N., Le Tron, P.Y., Reverdin, G., 2000. Global high-resolution mapping of ocean circulation from TOPEX/Poseidon and ERS-1& 2. J. Geophys. Res. 105, 19477–19498.

Ehrendorfer, M., Tribbia, J.J., 1997. Optimal prediction of forecast error covariances through singular vectors. J. Atmos. Sci. 54, 286–313.

Elliott, B.A., 1982. Anti-cyclonic rings in the Gulf of Mexico. J. Phys. Oceanogr. 12, 1292–1309.

Evensen, G., 1994. Sequential data assimilation with a nonlinear quasi-geostrophic model using Monte Carlo methods to forecast error statistics. J. Geophys. Res. 99, 10143–10162.

Ezer, T., Mellor, G.L., 1994. Continuous assimilation of Geosat altimeter data into a three-dimensional primitive equation Gulf Stream model. J. Phys. Oceanogr. 24 (4), 832–847.

Ezer, T., Oey, L.-Y., Sturges, W., Lee, H.-C., 2003. The variability of currents in the Yucatan Channel: analysis of results from a numerical ocean model, J. Geophys. Res., 10.1029/2002JC001509.

Fan, S.J., Oey, L.-Y., Hamilton, P., 2004. Assimilation of drifters and satellite data in a circulation model of the northeastern Gulf of Mexico. Cont. Shelf Res. 24 (9), 1001–1013.

Forristal, G.Z., Schaudt, K.J., Cooper, C.K., 1992. Evolution and kinematics of a Loop Current eddy in the Gulf of Mexico during 1985. J. Geophys. Res. 97, 2173–2184.

Johns, W.E., Townsend, T.L., Fratantoni, D.M., Wilson, W.D., 2002. On the Atlantic inflow to the Caribbean Sea. Deep Sea Res. 49, 211–243.

Kalnay, E., 2003. Atmospheric Modeling, Data Assimilation and Predictability. Cambridge University Press, New York, 341 pp.

Kamachi, M. et al., 2004. Short-Range Prediction Experiments with Operational Data Assimilation System for the Kuroshio South of Japan. J. Oceanogr. Soc. Jpn. 60, 269–282.

Kundu, P., 1976. An analysis of inertial oscillations observed near Oregon coast. J. Phys. Oceanogr. 6, 879–893.

Large, W.G., Pond, S., 1981. Open ocean flux measurements in moderate to strong winds. J. Phys. Oceanogr. 11, 324–336.

Leben, R.R., 2005. Altimeter-derived Loop Current metrics. In: Sturges, W., Lugo-Fernandez, A. (Eds.), Circulation in the Gulf of Mexico: Observations and Models, Geophysical Monograph Series, vol. 161. 360 pp.
Leipper, D.F., Volgenau, D., 1972. Hurricane heat potential of the Gulf of Mexico. J. Phys. Oceanogr. 2, 218–224.
Leith, C.E., 1974. Theoretical skill of Monte Carlo forecasts. Mon. Wea. Rev. 102, 409–418.
Lin, X.-H., Oey, L.-Y. and Wang, D.-P., in press. Altimetry and drifter data assimilations of Loop Current and eddies. J. Geophys. Res.
Lorenz, E.N., 1963. Deterministic non-periodic flow. J. Atmos. Sci. 20, 130–141.
Lorenz, E.N., 1965. A study of the predictability of a 28-variable atmospheric model. Tellus 17, 321–333.
Lorenz, E.N., 1993. The Essence of Chaos. University of Washington Press, Seattle.
MacKinnon, J.A., Gregg, M.C., 2003. Shear and baroclinic energy flux on the summer New England shelf. J. Phys. Oceanogr. 33, 1462–1475.
Mellor, G.L., 2001. One-dimensional, ocean surface layer modeling: a problem and a solution. J. Phys. Oceanogr. 31, 790–809.
Mellor, G.L., 2004. User s guide for a three-dimensional primitive equation numerical ocean model. In: Program in Atmospheric and Oceanic Sciences. Princeton University, 42 pp.
Mellor, G.L., Ezer, T., 1991. A Gulf Stream model and an altimetry assimilation scheme. J. Geophys. Res. 96, 8779–8795.
Mellor, G.L., Yamada, T., 1982. Development of a turbulence closure model for geophysical fluid problems. Rev. Geophys. Space Phys. 20, 851–875.
Miyazawa, Y., Yamane, S., Guo, X., Yamagata, T., 2005. Ensemble forecast of the Kuroshio meandering. J. Geophys. Res. 110, C10026. doi:10.1029/2004JC002426.
Moon, I.-J., Ginis, I., Hara, T., 2004. Effect of surface waves on Charnock coefficient under tropical cyclones. Geophys. Res. Lett. 31, L20302. doi:10.1029/2004GL020988.
Nowlin Jr., W.D., 1972. Winter circulation pattern and property distributions. In: Capurro, L.R.A., Reid, J.L. (Eds.), . In: Contributions on the Physical Oceanography of the Gulf of Mexico, vol. II. Gulf Publishing Co, pp. 3–64.
Oey, L.-Y., 1995. Eddy- and wind-forced shelf circulation. J. Geophys. Res. 100, 8621–8637.
Oey, L.-Y., 1996. Simulation of mesoscale variability in the Gulf of Mexico. J. Phys. Oceanogr. 26, 145–175.
Oey, L.-Y., 2004. Vorticity flux in the Yucatan Channel and loop current eddy shedding in the Gulf of Mexico. J. Geophys. Res. 109, C10004. doi:10.1029/2004JC002400.
Oey, L.-Y., Chen, P., 1992. A model simulation of circulation in the north-east Atlantic shelves and seas. J. Geophys. Res. 97, 20087–20115.
Oey, L.-Y., Lee, H.-C., 2002. Deep eddy energy and topographic Rossby waves in the Gulf of Mexico. J. Phys. Oceanogr. 32, 3499–3527.
Oey, L.-Y., Zhang, H.-C., 2004. A mechanism for the generation of subsurface cyclones and jets. Cont. Shelf Res. 24, 2109–2131.
Oey, L.-Y., Lee, H.-C., Schmitz Jr., W.J., 2003. Effects of winds and Caribbean Eddies on the frequency of loop current eddy shedding: A Numerical Model Study. J. Geophys. Res. 108 (C10), 3324. doi:10.1029/2002JC001698.
Oey, L.-Y., Ezer, T., Sturges, T., 2004. Modeled and observed empirical orthogonal functions of currents in the Yucatan Channel. J. Geophys. Res. 109, C08011. doi:10.1029/2004JC002345.
Oey, L.-Y., Ezer, T., & Lee, H.J., 2005a. Loop current, rings and related circulation in the Gulf of Mexico: A review of numerical models and future challenges. In: Sturges, W., Lugo-Fernandez, A., (Eds.), Circulation in the Gulf of Mexico: Observations and Models, Geophysical Monograph Series, vol. 161. 360 pp, 2005.
Oey, L.-Y., Ezer, T., Forristall, G., Cooper, C., DiMarco, S., Fan, S., 2005b. An exercise in forecasting loop current and eddy frontal positions in the Gulf of Mexico. Geophys. Res. Lett. 32, L12611. doi:10.1029/2005GL023253.
Oey, L.-Y., Ezer, T., Wang, D.-P., Fan, S.-J., Yin, X.-Q., 2006. Loop Current warming by Hurricane Wilma. Geophys. Res. Lett. 33, L08613. doi:10.1029/ 2006GL025873.
Oey, L.-Y., Ezer, T., Wang, D.-P., Yin, X.-Q. and Fan, S.-J., in press. Hurricane-induced motions and interaction with ocean currents, Cont. Shelf Res. doi:10.1016/j.csr.2007.01.008.
Oke, P. et al., 2002. A modeling study of the three-dimensional continental shelf circulation off Oregon. Part I: Model-data comparisons. J. Phys. Oceanogr. 32, 1360–1382.
Paduan, J.D., Shulman, I., 2004. HF radar data assimilation in the Monterey Bay area. J. Geophys. Res., Ocean 109, C07S09. doi:10.1029/2003JC001949.
Palmen, E., 1948. On the formation and structure of tropical cyclones. Geophysics 3, 26–38.
Powell, M.D., Vickery, P.J., Reinhold, T., 2003. Reduced drag coefficient for high wind speeds in tropical cyclones. Nature 422, 279–283.
Price, J.F., 1981. Upper Ocean Response to a Hurricane. J. Phys. Oceanogr. 11, 153–175.
Scharroo, R., Smith, W.H.F., Lillibridge, J.L., 2005. Satellite altimetry and the intensification of Hurricane Katrina. EOS Trans. 86 (40), 366.
Sheinbaum, J., Candela, J., Badan, A., Ochoa, J., 2002. Flow structure and transports in the Yucatan Channel. Geophys. Res. Let. 29 (3). doi:10.1029/2001GL0139990.
Sturges, W., Leben, R., 2000. Frequency of ring separations from the Loop Current In the Gulf of Mexico: A revised estimate. J. Phys. Oceanogr. 30, 1814–1818.
Toth, Z., Kalnay, E., 1993. Ensemble forecasting at NMC: The generation of perturbations. Bull. Amer. Met. Soc. 74 (12), 2317–2330.
Toth, Z., Kalnay, E., 1997. Ensemble forecasting at NCEP and the breeding method. Mon. Wea. Rev. 125, 3297–3319.
Vukovich, F.M., 1995. An updated evaluation of the Loop Currents eddy-shedding frequency. J. Geophys. Res. 100, 8655–8659.
Vukovich, F.M., Crissman, B.W., 1986. Aspects of warm rings in the Gulf of Mexico. J. Geophys. Res. 91, 2645–2660.
Wang, D.-P., 1993. Model of frontogenesis: subduction and upwelling. J. Mar. Res. 51, 497–513.
Wang, D.-P., Oey, L.-Y., Ezer, T., Hamilton, P., 2003. Nearsurface currents in DeSoto Canyon. J. Phys. Oceanogr. 33, 313–326.
Yang, S.-C., Cai, M., Kalnay, E., Rienecker, M., Yuan, G., Toth, Z., 2006. ENSO bred vectors in coupled ocean-atmosphere general circulation models. J. Climate 19, 1422–1436.